Monthly Notices of the ROYAL ASTRONOMICAL SOCIETY

MNRAS **499,** 1266–1286 (2020)
Advance Access publication 2020 September 18

doi:10.1093/mnras/staa2817

Tracking the year-to-year variation in the spectral energy distribution of the narrow-line Seyfert 1 galaxy Mrk 335

S. Tripathi,[1]★ K. M. McGrath,[1] L. C. Gallo,[1] D. Grupe,[2] S. Komossa,[3] M. Berton ,[4,5] G. Kriss [6] and A. L. Longinotti[7]

[1]*Department of Astronomy and Physics, Saint Mary's University, 923 Robie Street, Halifax, NS B3H 3C3, Canada*
[2]*Space Science Center, Morehead State University, 235 Martindale Drive, Morehead, KY 40351, USA*
[3]*Max-Planck-Institut für Radioastronomie, Auf dem Hügel 69, D-53121 Bonn, Germany*
[4]*Finnish Centre for Astronomy with ESO (FINCA), University of Turku, Quantum, Vesilinnantie 5, FI-20014 Turku, Finland*
[5]*Metsähovi Radio Observatory, Aalto University, Metsähovintie 114, FI-02540 Kylmälä, Finland*
[6]*Space Telescope Science Institute, 3700 S. Martin Drive, Baltimore, MD 21218, USA*
[7]*CONACyT–Instituto Nacional de Astrofísica, Óptica y Electrónica, Luis E. Erro 1, Tonantzintla, 72840, Puebla, México*

Accepted 2020 September 11. Received 2020 August 28; in original form 2020 April 27

ABSTRACT

Multiwavelength monitoring of Mrk 335 with *Swift* between 2007 and 2019 are used to construct annual spectral energy distributions (SEDs) and track year-to-year changes. Non-contemporaneous archival data prior to 2007 are used to build a bright state SED. In this work, the changes are examined and quantified to build the foundation for future SED modelling. The yearly SEDs trace a downward trend on the average, with the X-ray portion varying significantly and acquiring further lower values in the past two years when compared to the optical/UV portion of SED. The bolometric Eddington ratios derived using optical/UV to X-ray SEDs and the calculated X-ray luminosities show a gradual decrease over the monitoring period. Changes in the parameters over time are examined. Principal component analysis suggests that the primary variability is in the X-ray properties of Mrk 335. When looking at the broader picture of Mrk 335 and its behaviour, the X-rays, accounting most of the variability in the 13-yr data, are possibly driven by physical processes related to the corona or absorption whereas the modest optical–UV variations suggest their origin within the accretion disc. These results are consistent with the previous interpretation of Mrk 335 using the timing analyses on the monitoring data and spectral modelling of deep observations.

Key words: galaxies: active – galaxies: individual: Mrk 335 – galaxies: nuclei – X-rays: galaxies.

1 INTRODUCTION

The narrow-line Seyfert 1 galaxy (NLS1; e.g. Osterbrock & Pogge 1985; Komossa 2008; Gallo 2018) Mrk 335 ($z = 0.025$) has revealed variations in the flux and spectral shape during recent years that makes it as one of the remarkable sources for the investigation of the nature of corona and the accretion disc. Mrk 335 displayed an intriguing behaviour when it switched from, being a typical bright 'normal' active galactic nucleus (AGN) over decades, to an abruptly low-flux system in 2007 (Grupe, Komossa & Gallo 2007). The historic flux drop which was about one-thirtieth of its typical bright flux state, immediately gathered attention to carefully investigate the source, resulting in the *Swift* monitoring as well as several deep follow-up observations with *XMM–Newton*, *Suzaku*, *NuSTAR*, and *HST* since 2007 (e.g. Grupe et al. 2008; Longinotti et al. 2008, 2013, 2019; Wilkins et al. 2015; Gallo et al. 2013, 2015, 2018, 2019; Parker et al. 2014, 2019; Wilkins & Gallo 2015). Various follow-up studies indicate that the source has never reverted to its former bright state. It is usually at one-tenth its previous brightness with occasional episodes of intense flaring by factors of 10 (Grupe, Gallo & Komossa 2014) and deep flux drops (Grupe et al. 2015). The source exhibits high variability in the X-rays roughly by a factor of 50, while only a factor of 2–3 variations is seen in the simultaneous UV light curves. Mrk 335 is currently in an X-ray weak state (Grupe, Komossa & Gallo 2018a; Grupe et al. 2018b) compared to its UV brightness and continues to be monitored by *Swift* so to understand the cause of the prolonged dim state and the intermittent high amplitude flaring activity. In 2020 June, Mrk 335 exhibited rapid brightening after nearly 2 yr in relative quiescence (Grupe, Komossa & Gallo 2020). These data are presented in Komossa et al. (in preparation) and are not included in this work.

Gallo et al. (2018) performed the structure function analysis on the elapsed 11 years' *Swift* optical/UV and X-ray data of Mrk 335. The objective was to incorporate the structure function technique to characterize the optical/UV emission on the simultaneous but unevenly sampled multiwavelength data. The study showed that the long dimmed X-ray state and the corresponding optical/UV emission favourably respond to different processes. The X-ray low-flux state could be attributed to the physical changes in the corona or absorption, whereas the variability in the optical/UV band is more consistent with the thermal and dynamic time-scales associated with the accretion disc.

Also, the extended dim X-ray phase is not accompanied by the corresponding similar substantial variability or dimness in the optical/UV band. The optical/UV emission, on average, remain

★ E-mail: shruti020p@gmail.com

consistent with the measurements obtained prior to 2007, i.e. bright state (e.g. Peterson et al. 1998; Grupe et al. 2012; Komossa et al. 2014); varying by relatively small amplitude by about a factor of 2. This results in the X-ray weak state of Mrk 335 compared to its UV luminosity (e.g. Gallo 2006). Several studies have attempted to explain the cause of the X-ray dimming in Mrk 335. One explanation could be due to the collapse of the corona to form a possible collimated structure (e.g. Gallo et al. 2013, 2015; Wilkins & Gallo 2015; Wilkins et al. 2015) or due to absorption processes and partial obscuration of the corona and the disc (e.g. Grupe et al. 2008; Longinotti et al. 2013, 2019). Blurred reflection scenario favour some flux states of Mrk 335 where the reverberation lags are found (Kara et al. 2013). Partial covering scenario, too, can explain the dimness, but is unable to sef-consistently describe both the low- and high-flux broad-band emission from the source (Gallo et al. 2015). Absorption does play a role in Mrk 335 (e.g. Longinotti et al. 2013, 2019; Parker et al. 2019) on some level.

The first 5 and the 11 yr of the monitoring campaign are presented by Grupe et al. (2012) and Gallo et al. (2018), respectively (see also Buisson et al. 2017). Gallo et al. (2018) have examined the power spectra and characteristic time-scales for the 11-yr period of simultaneous multiwavelength optical/UV and X-ray data. However, these multiwavelength data have not been examined for the spectral energy distribution (SED) and the spectral variability analyses.

In this work, we look at the available multiwavelength data post-2007 of Mrk 335 with the goal of characterizing the changes in the SED in the NLS1. The annual SED measurements can give physical insight to the changes in the accretion disc leading to changes in the simultaneous UV emission. In addition, this allows to investigate the physical parameters that drive the variations in the X-rays. Through this approach, we aim to search for correlations amongst its key SED parameters and the multiwavelength properties over more than a decade, test for comparison of these parameters to that of a representative high state of Mrk 335, and thereby, to understand the rudimentary physical processes responsible for the low-flux characteristics of Mrk 335.

The following section features all the available multiwavelength observations and the data reduction procedure. Section 3 describes the variations in the optical and UV data. X-ray variability of Mrk 335 is discussed in the Section 4. Section 5 is split into the time-resolved and flux-resolved methods of SED measurements, respectively. Correlations between all the measured multiwavelength parameters of Mrk 335 are investigated and the statistical analysis using principal component analysis (PCA) is performed to describe the behaviour of Mrk 335 over the extended 13-yr period in Section 6. Discussion and conclusions follow in Sections 7 and 8, respectively.

2 OBSERVATIONS AND DATA REDUCTION

2.1 X-ray data analysis

In this work, we study all the *Swift* observations starting from 2007 to 2019 year-wise in Table 1. The new Swift observations between 2018 May and 2019 October are listed in Table 2. The X-ray and UV measurements for these observations are shown in Table 3. Previous observations have been discussed in Grupe et al. (2012) and Gallo et al. (2018). Mrk 335 has been monitored on a regular basis since 2007 when it was discovered by *Swift* to be in an extreme X-ray low state (Grupe et al. 2007). Due to its sun constraint, Mrk 335 cannot be observed by *Swift* between February and May.

All X-ray observations were obtained by the X-ray Telescope (XRT; Burrows et al. 2005) on board *Swift* and were performed in the photon counting (pc) mode (Hill et al. 2004). Data corresponding to each epoch in Table 1 were used to generate X-ray spectrum, background spectrum, response, and auxiliary response files (ARF). The processing followed standard methods:

Table 1. Average yearly *Swift* XRT observations of Mrk 335.

Epoch	Time interval
Year 0	<2007
Year 1	2007–05 to 2008–01
Year 2	2008–06 to 2009–02
Year 3	2009–05 to 2010–02
Year 4	2010–05 to 2011–01
Year 5	2011–05 to 2012–02
Year 6	2012–05 to 2013–02
Year 7	2013–05 to 2014–02
Year 8	2014–05 to 2015–02
Year 9	2015–05 to 2016–02
Year 10	2016–05 to 2017–02
Year 11	2017–05 to 2018–02
Year 12	2018–05 to 2019–02
Year 13	2019–05 to 2019–09

(i) Data reduction is performed with *xrtpipeline* which is a part of the HEASOFT software package.

(ii) Extraction of source and background spectra and event files in circular regions with radii of 94″ and 295″, respectively, using XSELECT.

(iii) Creating auxiliary response files (ARF) for each spectrum using the FTOOL *xrtmkarf*.

(iv) Due to the low number of counts we use a binning of 1 within the FTOOL *grppha*. We also linked the most recent response file *swxpc0to12s6_20130101v014.rmf* to the spectrum.

(v) All spectra were analysed by the XSPEC version 12.9.1 (Arnaud 1996) using Cash Statistics (Cash 1979).

(vi) Count rates were determined using the online *Swift* XRT product tool at the *Swift* data centre in Leicester.[1]

(vii) Hardness ratios were defined as $\mathrm{HR} = \frac{\mathrm{hard-soft}}{\mathrm{hard+soft}}$ where *soft* and *hard* are the counts in the 0.3–1.0 and 1.0–10 keV bands, respectively, and determined by the Bayesian statistics software BEHR[2] by Park et al. (2006).

The *Swift*'s UV-Optical Telescope (UVOT; Roming et al. 2005) was performed as follows:

(i) In each filter each observation was co-added using the UVOT task *uvotimsum*.

(ii) Region files had a circular region with radii of 5″ and 20″ for the source and background data, respectively.

(iii) Fluxes and magnitudes were measured using the uvottool *uvotsource* which is based on the most recent calibration as described in Poole et al. (2008) and Breeveld et al. (2010).

(iv) All magnitudes and fluxes used in this publication are corrected for Galactic reddening [$E(B-V) = 0.035$; Schlegel, Finkbeiner & Davis 1998], using equation 2 in Roming et al. (2009) applying the reddening curves given in Cardelli, Clayton & Mathis (1989). The correcting magnitudes corresponding to each UVOT filter are shown in Table 4.

[1] https://www.swift.ac.uk/user_objects/
[2] http://hea-www.harvard.edu/AstroStat/BEHR/

Table 2. *Swift* XRT and UVOT observations of Mrk 335 since 2018 February. All exposure times are given in seconds. Previous observations are listed in Grupe et al. (2008, 2012) and Gallo et al. (2018). All observations had the target ID 33420. The full list of observations is shown online. The MJD is given in the middle of an observation.

Segment	MJD[1]	$T_{\rm start}$ (UT)	$T_{\rm end}$ (UT)	$T_{\rm exp,\,XRT}$	$T_{\rm exp,\,V}$	$T_{\rm exp,\,B}$	$T_{\rm exp,\,U}$	$T_{\rm exp,\,W1}$	$T_{\rm exp,\,M2}$	$T_{\rm exp,\,W2}$
151	58163.203	2018-02-14 04:41	2018-02-14 05:01	1226	–	–	–	–	–	1226
153	58267.401	2018-05-29 09:30	2018-05-29 09:45	869	–	–	–	–	–	858
154	58269.007	2018-05-31 00:03	2018-05-31 00:18	829	–	–	–	–	–	963
155	58280.691	2018-06-11 16:28	2018-06-11 16:41	727	–	–	–	–	–	716
158	58293.588	2018-06-24 14:02	2018-06-24 14:12	564	–	–	–	–	–	557
159	58301.417	2018-07-02 09:53	2018-07-02 10:07	812	–	–	–	–	–	812
160	58307.761	2018-07-08 17:26	2018-07-08 19:05	1039	82	82	82	165	236	330
161	58309.244	2018-07-10 05:43	2018-07-10 06:00	1026	83	83	83	166	240	333
162	58310.038	2018-07-11 09:01	2018-07-11 09:15	829	83	83	83	167	45	334
163	58311.107	2018-07-12 02:26	2018-07-12 02:44	1044	84	84	84	168	250	336

Table 3. *Swift* XRT and UVOT measurements of Mrk 335 since 2018 February. The XRT count rates are given in units of counts s^{-1}. The hardness ratios are defined as HR $= \frac{\rm hard-soft}{\rm hard+soft}$, where soft and hard are the counts in the 0.3–1.0 and 1.0–10.0 keV bands, respectively. The reddening corrected UVOT magnitudes are in the Vega system. The full list of observations is shown online.

MJD	XRT CR	XRT HR	*V*	*B*	*U*	UVW1	UVM2	UVW2
58163.203	0.055 ± 0.008	-0.04 ± 0.12	–	–	–	–	–	13.51 ± 0.03
58267.401	0.044 ± 0.008	-0.10 ± 0.12	–	–	–	–	–	13.65 ± 0.04
58269.007	0.049 ± 0.008	-0.18 ± 0.14	–	–	–	–	–	13.67 ± 0.04
58280.691	0.052 ± 0.009	-0.27 ± 0.18	–	–	–	–	–	13.65 ± 0.04
58293.588	0.056 ± 0.011	-0.18 ± 0.20	–	–	–	–	–	13.80 ± 0.04
58301.417	0.052 ± 0.009	-0.39 ± 0.16	–	–	–	–	–	13.86 ± 0.04
58307.761	0.054 ± 0.008	-0.28 ± 0.14	14.62 ± 0.04	14.91 ± 0.04	13.74 ± 0.04	13.68 ± 0.04	13.73 ± 0.04	13.83 ± 0.04
58309.244	0.063 ± 0.008	-0.07 ± 0.15	14.56 ± 0.04	14.89 ± 0.04	13.77 ± 0.04	13.67 ± 0.04	13.67 ± 0.04	13.81 ± 0.04
58310.038	0.043 ± 0.008	-0.13 ± 0.18	14.58 ± 0.04	14.88 ± 0.04	13.72 ± 0.04	13.71 ± 0.04	13.65 ± 0.04	13.82 ± 0.04
58311.107	0.051 ± 0.008	-0.21 ± 0.16	14.55 ± 0.04	14.88 ± 0.04	13.72 ± 0.04	13.68 ± 0.04	13.71 ± 0.04	13.81 ± 0.04

Table 4. Correcting magnitudes of UVOT filters.

UVOT filter	Correction
V-corr	0.1166
B-corr	0.1519
U-corr	0.1908
UVW1-cor	0.2394
UVM2-corr	0.3413
UVW2-corr	0.2867

Table 5. Summary of optical observations of Mrk 335.

Observatory	Number of observations	Date
HST/FOS	1	1994-12-16
MDM	78	2010-08-31 to 2010-12-28
ASIAGO	4	2014-09-23 to 2018-07-07

2.2 Optical spectroscopy

Optical spectral data used in this work are listed in Table 5. Data covering the wavelength range 1152–6072 Å were obtained from the *HST* Faint Object Spectrograph (FOS) and are representative of the bright state prior to 2007. We have 78 spectra obtained with MDM Observatory 1.3 m McGraw-Hill telescope on Kitt Peak and the data processing is described in Grier et al. (2012). The target was observed multiple times with the 1.22 m telescope of the Asiago Astrophysical Observatory (Italy) using the Boller & Chivens spectrograph with a 300 mm^{-1} grating. The spectra have a dispersion of 2.6 Å $pixel^{-1}$ and an instrumental resolution of ∼700. The spectra were reduced using standard IRAF tools. The data were first corrected for bias and flat-field, and then calibrated in wavelength and flux.

Table 6. Ultraviolet observations of Mrk 335.

Instrument	Grating/tilt	Date	Wavelength studied
FUSE	–	1999	912–1186 Å
FUSE	–	2000	912–1186 Å
HST STIS	E140M	2004-07-01	1125–1425 Å
HST COS	G160M	2009-10-31	1421–1810 Å
HST COS	G160M	2010-02-08	1421–1795 Å
HST COS	G130M	2010-02-08	1135–1425 Å
HST COS	G160M	2016-01-04	900–1150 Å
HST COS	G140L	2016-01-04/-07	900–2150 Å
HST COS	G130M	2016-01-04	1110–1425 Å
HST COS	G160M	2018-07-24	1390–1750 Å
HST COS	G130M	2018-07-23	1110–1390 Å

2.3 Ultraviolet spectroscopy

Ultraviolet observations of Mrk 335 representing the bright state are from the Far Ultraviolet Spectroscopic Explorer (FUSE) and *HST* Space Telescope Imaging Spectrograph (STIS). *HST* cosmic origins spectrograph (COS) data between 2010–2018 are used for the dim state. The detailed analysis of these observations have been done by Longinotti et al. (2013, 2019) and Parker et al. (2019). The UV observation log is shown in Table 6.

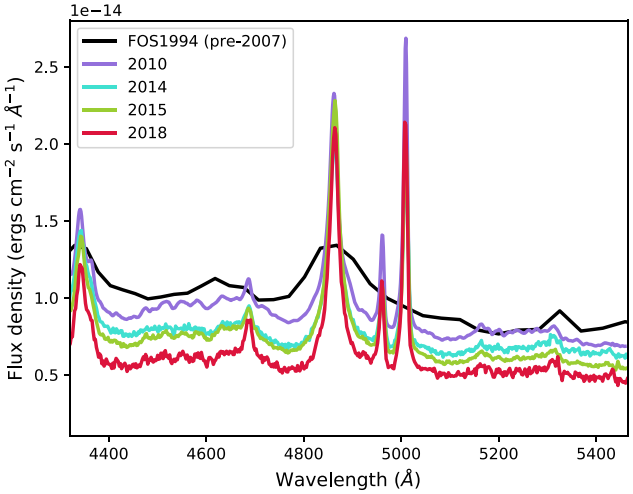

Figure 1. Variations in the H β spectral region between 1994 and 2018 are on the same order as the more rapid changes (Grier et al. 2012), but show a general downward trend, from 1994 (bright state) to 2018. The 1994 FOS data are of lower resolution compared to the other spectra.

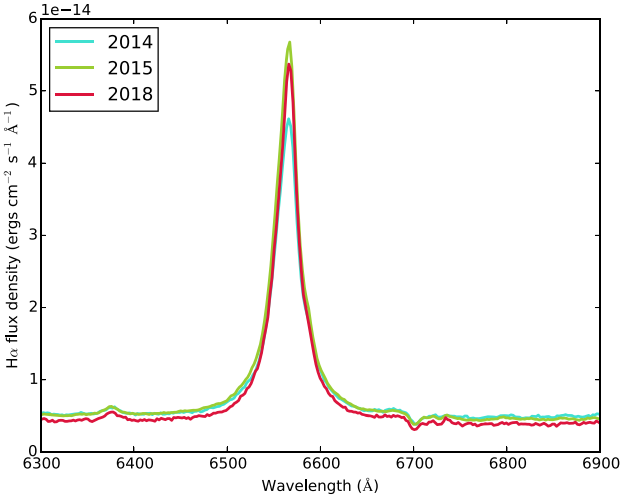

Figure 2. Variations in the H α line from 2014 to 2018 appear to be less significant than in H β.

3 OPTICAL AND UV VARIABILITY

The available optical and ultraviolet observations of Mrk 335 have been studied in the past (e.g. Grier et al. 2012; Longinotti et al. 2013, 2019). In this section, we quantify the average behaviour of flux variations in the optical/UV data of the source over several years.

3.1 Optical variability

The spectra of 78 observations show a general decrease in the flux with time (Grier et al. 2012). An average change in the flux density is noted at 20 per cent level over a shorter time span of 4 months (∼120 d). In Fig. 1, the variations in the flux density for all the optical spectra in the H β spectral region are presented which span longer time-scales (∼20 yr). For these observations, we notice a general downward trend in the flux consistently, from the bright state in 1994 to the low-flux state in 2018. The spectra were also plotted in

Table 7. Year-wise measurements of Mrk 335 since 2007 January. The XRT values are in units of counts s^{-1}. The hardness ratio is defined as HR $= \frac{\text{hard}-\text{soft}}{\text{hard}+\text{soft}}$, where soft and hard are the counts in the 0.3–1.0 and 1.0–10.0 keV bands, respectively.

Year	kT (eV)	$kT_{\rm norm}$ [a]	Γ	$\Gamma_{\rm norm}$ [b]	HR	$F_{\rm var}$	$F_{2\,\rm kev}$ [c]	$L_{\rm t}/L_{\rm Bol}$	$\alpha_{\rm ox}$	SE $\times 10^{-1}$	$L_{\rm Bol}/L_{\rm Edd}$	$\alpha_{\rm uv}$	$F_{\rm varUV}$	F_{2500} [d]
Year 0	99 ± 1	1.30 ± 0.04	2.42 ± 0.01	$10.31^{+0.04}_{-0.05}$	0.08 ± 0.01	0.12 ± 0.01	2.61 ± 0.01	0.05 ± 0.02	− 1.30 ± 0.02	10.57 ± 0.01	0.18	0.5 ± 0.04	–	6.8 ± 0.4
Year 1	109 ± 2	0.94 ± 0.03	1.65 ± 0.03	1.88 ± 0.06	0.30 ± 0.01	0.73 ± 0.10	0.82 ± 0.02	0.03 ± 0.02	− 1.47 ± 0.01	9.77 ± 0.02	0.12	0.4 ± 0.1	0.09 ± 0.02	5.5 ± 0.01
Year 2	109 ± 3	1.10 ± 0.05	1.91 ± 0.03	3.65 ± 0.09	0.25 ± 0.01	0.37 ± 0.15	1.33 ± 0.03	0.04 ± 0.01	− 1.53 ± 0.01	10.05 ± 0.03	0.12	0.4 ± 0.1	0.09 ± 0.05	5.2 ± 0.1
Year 3	110 ± 3	0.45 ± 0.02	1.21 ± 0.05	$0.70^{+0.04}_{-0.03}$	0.52 ± 0.01	0.62 ± 0.07	0.41 ± 0.02	0.03 ± 0.03	− 1.57 ± 0.02	9.63 ± 0.03	0.10	0.4 ± 0.1	0.12 ± 0.01	5.2 ± 0.1
Year 4	117 ± 7	0.60 ± 0.06	1.32 ± 0.11	0.97 ± 0.11	0.44 ± 0.02	0.68 ± 0.04	0.53 ± 0.05	0.04 ± 0.02	− 1.36 ± 0.04	9.65 ± 0.07	0.10	0.4 ± 0.1	0.21 ± 0.01	4.6 ± 0.01
Year 5	111 ± 3	0.73 ± 0.03	1.57 ± 0.04	1.10 ± 0.05	0.27 ± 0.01	0.86 ± 0.08	0.50 ± 0.02	0.03 ± 0.01	− 1.52 ± 0.01	9.68 ± 0.03	0.10	0.6 ± 0.1	0.17 ± 0.02	4.6 ± 0.01
Year 6	103 ± 4	0.47 ± 0.03	1.34 ± 0.06	0.67 ± 0.04	0.42 ± 0.01	0.70 ± 0.09	0.38 ± 0.02	0.02 ± 0.01	− 1.58 ± 0.02	9.64 ± 0.04	0.10	0.4 ± 0.1	0.09 ± 0.01	4.9 ± 0.1
Year 7	108 ± 3	0.27 ± 0.01	0.93 ± 0.05	0.31 ± 0.02	0.59 ± 0.01	0.64 ± 0.06	0.21 ± 0.01	0.02 ± 0.01	− 1.68 ± 0.02	9.49 ± 0.03	0.10	0.4 ± 0.2	0.07 ± 0.01	5.2 ± 0.01
Year 8	118 ± 4	0.36 ± 0.02	0.96 ± 0.08	0.34 ± 0.03	$0.51^{+0.01}_{-0.02}$	1.14 ± 0.11	0.24 ± 0.02	0.02 ± 0.01	− 1.69 ± 0.03	9.41 ± 0.05	0.11	0.3 ± 0.2	0.13 ± 0.01	5.9 ± 0.01
Year 9	102 ± 3	0.53 ± 0.03	1.27 ± 0.06	0.63 ± 0.04	0.42 ± 0.01	0.66 ± 0.08	0.35 ± 0.02	0.03 ± 0.03	− 1.53 ± 0.02	9.57 ± 0.04	0.08	0.4 ± 0.1	0.24 ± 0.03	3.5 ± 0.01
Year 10	103 ± 4	0.34 ± 0.02	1.10 ± 0.07	0.37 ± 0.03	$0.50^{+0.02}_{-0.01}$	0.78 ± 0.08	0.24 ± 0.02	0.03 ± 0.02	− 1.60 ± 0.03	9.49 ± 0.04	0.07	0.4 ± 0.1	0.15 ± 0.02	3.6 ± 0.01
Year 11	107 ± 4	0.39 ± 0.02	1.26 ± 0.07	0.48 ± 0.03	$0.42^{+0.02}_{-0.01}$	0.88 ± 0.10	0.28 ± 0.02	0.03 ± 0.02	− 1.57 ± 0.03	9.57 ± 0.04	0.07	0.4 ± 0.1	0.11 ± 0.01	3.5 ± 0.1
Year 12	147 ± 8	0.10 ± 0.01	$0.59^{+0.26}_{-0.24}$	0.04 ± 0.01	$0.47^{+0.03}_{-0.04}$	0.15 ± 0.03	0.05 ± 0.01	0.01 ± 0.01	− 1.84 ± 0.06	9.13 ± 0.13	0.08	0.4 ± 0.1	0.07 ± 0.01	3.2 ± 0.01
Year 13	144 ± 15	0.10 ± 0.01	$0.34^{+0.46}_{-0.43}$	$0.04^{+0.03}_{-0.02}$	$0.59^{+0.03}_{-0.08}$	0.13 ± 0.08	0.02 ± 0.02	0.01 ± 0.02	− 2.03 ± 0.3	9.07 ± 0.20	0.07	0.2 ± 0.1	0.13 ± 0.02	3.9 ± 0.07

[a] $kT_{\rm norm}$ is in units of 10^{-4} ($R_{\rm in}$/km)/(D/10 kpc), where $R_{\rm in}$ is the inner radius and D is the distance. [b] $\Gamma_{\rm norm}$ is in units of 10^{-3} photons keV^{-1} cm^{-2} s^{-1} at 1 kev. [c] $F_{2\,\rm keV}$ is in units of μJy. [d] F_{2500} is in units of 10^{-26} erg cm^{-2} s^{-1} Hz^{-1}.

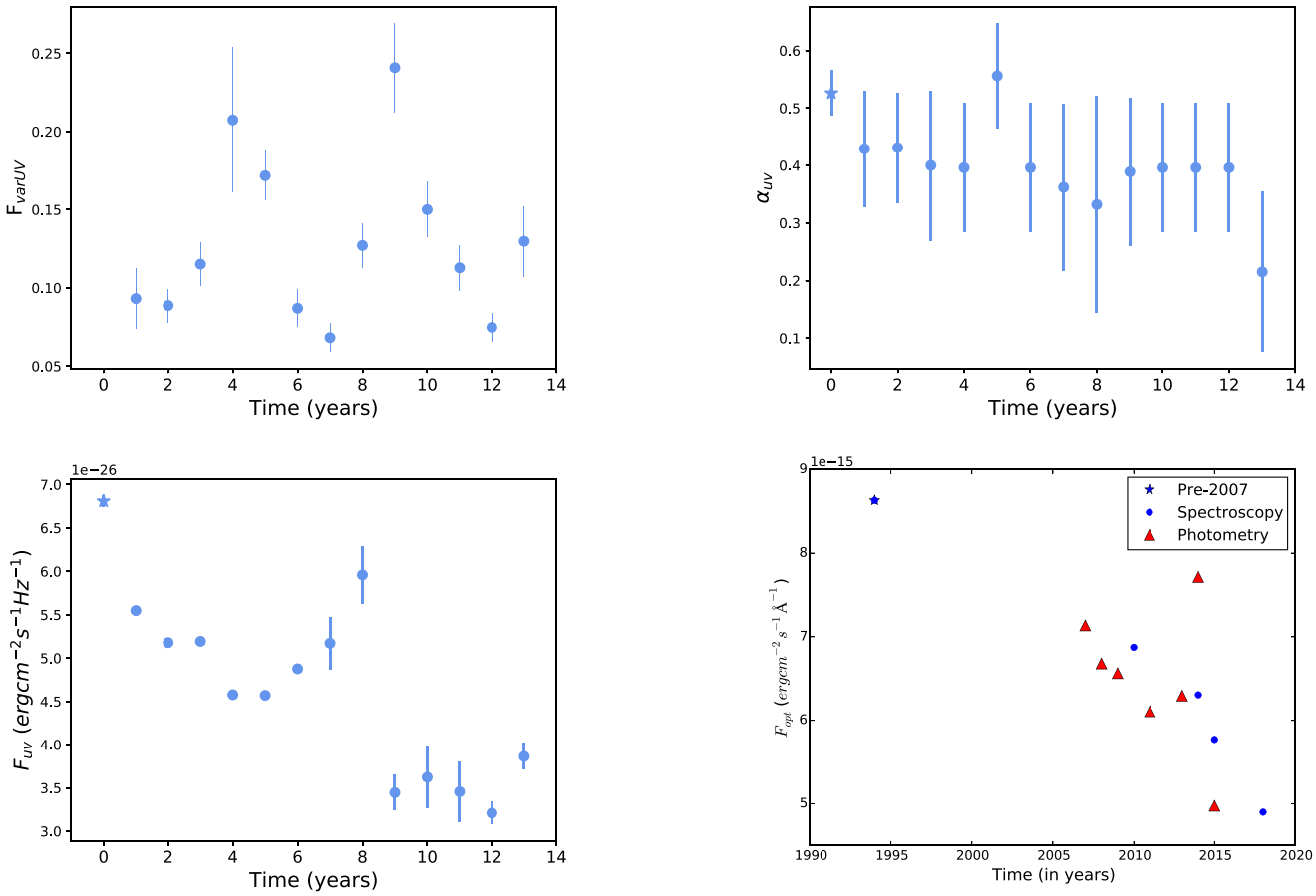

Figure 3. Top left: Variations of $F_{\rm varUV}$; top right: UV spectral slope $\alpha_{\rm UV}$; bottom left: flux density at 2500 Å ($F_{\rm uv}$); bottom right: flux density at 5100 Å ($F_{\rm opt}$) both obtained with spectroscopy and photometry over the years. Year 0 represents bright state of Mrk 335 and is represented by a 'star' symbol.

the Hα spectral region for the dim 4-yr period (2014–2018) which suggest modest variations in the flux as shown in Fig. 2.

3.2 UV spectral variability

The ultraviolet spectra in the Lyα region (∼1190–1225 Å) from 2004 (bright state) to 2018 span longer time-scales (∼14-yr). Measuring the average change in the flux density within the regions devoid of emission lines, it varies at less than 10 per cent level. Similarly, the average flux density in the O VI region (∼1015–1050 Å) and in the C IV region (∼1525–1575 Å) vary within 25 per cent and 20 per cent, respectively. The spectra show a general downward trend in brightness over time. It is to be noted that the optical photometric studies of Mrk 335 in 1995–2004 also revealed that the brightness of the source has decreased systematically over those years (Doroshenko et al. 2005). The detailed investigation of the variations in these line fluxes have been performed by Longinotti et al. (2013, 2019) and Parker et al. (2019).

3.3 Measured optical–UV parameters

We also measured optical and UV spectral parameters with the help of available spectroscopic and photometric data.

The UV spectral index $\alpha_{\rm uv}$ is measured from the power-law fitting of photometric data with six *Swift* UVOT filters. The typical value of $\alpha_{\rm uv}$ from our measurements is ∼−0.4, which is comparable to the index value −0.44 found for the SDSS spectra (Vanden Berk et al. 2001).

Flux densities at 2500 Å ($F_{\rm uv}$) were obtained with the UVW1 band centred at ∼2600 Å. Flux densities at 5100 Å ($F_{\rm opt}$) were obtained both using spectroscopic and photometric data. With photometry, $F_{\rm opt}$ was obtained using the V (∼ 5468 Å) or B (∼ 4392 Å) filters when available, otherwise by extrapolating the power law of $\alpha_{\rm uv}$.

The root-mean-squared fractional variability for the UVW2 (1928 Å) light curve ($F_{\rm varUV}$) during all epochs of the dim 13-yr period were computed using the equation of $F_{\rm var}$ described in Edelson et al. (2002), that quantifies the intrinsic variability of the light curve while accounting for uncertainty on the data points. That is,

$$F_{\rm var} = \sqrt{\frac{S^2 - \overline{\sigma_{\rm err}^2}}{\bar{x}^2}}. \quad (1)$$

where $S^2 - \overline{\sigma_{\rm err}^2}$ is the excess variance normalized by the mean count rate $\bar{x}$. S^2 is the light-curve variance and $\overline{\sigma_{\rm err}^2}$ is the mean square error due to flux measurements. This parameter allows to compare the amplitude of any variations present in a given energy band by calculating the standard deviation of counts to the average in that energy band.

Table 7 lists the measured UV parameters corresponding to each year. Average variations in these parameters with time are shown in Fig. 3. The $F_{\rm varUV}$ exhibits a range of variability amplitudes. Years 4, 5, 9, and 10 display large values of ∼15–25 per cent. Relatively low values of ∼7 per cent are measured in Years 7 and 12. The remaining years exhibit intermediate values. The UV spectral slope $\alpha_{\rm uv}$ is statistically constant over the observing period, but there is noticeable flattening from the high state (Year 0) to Year 1 and

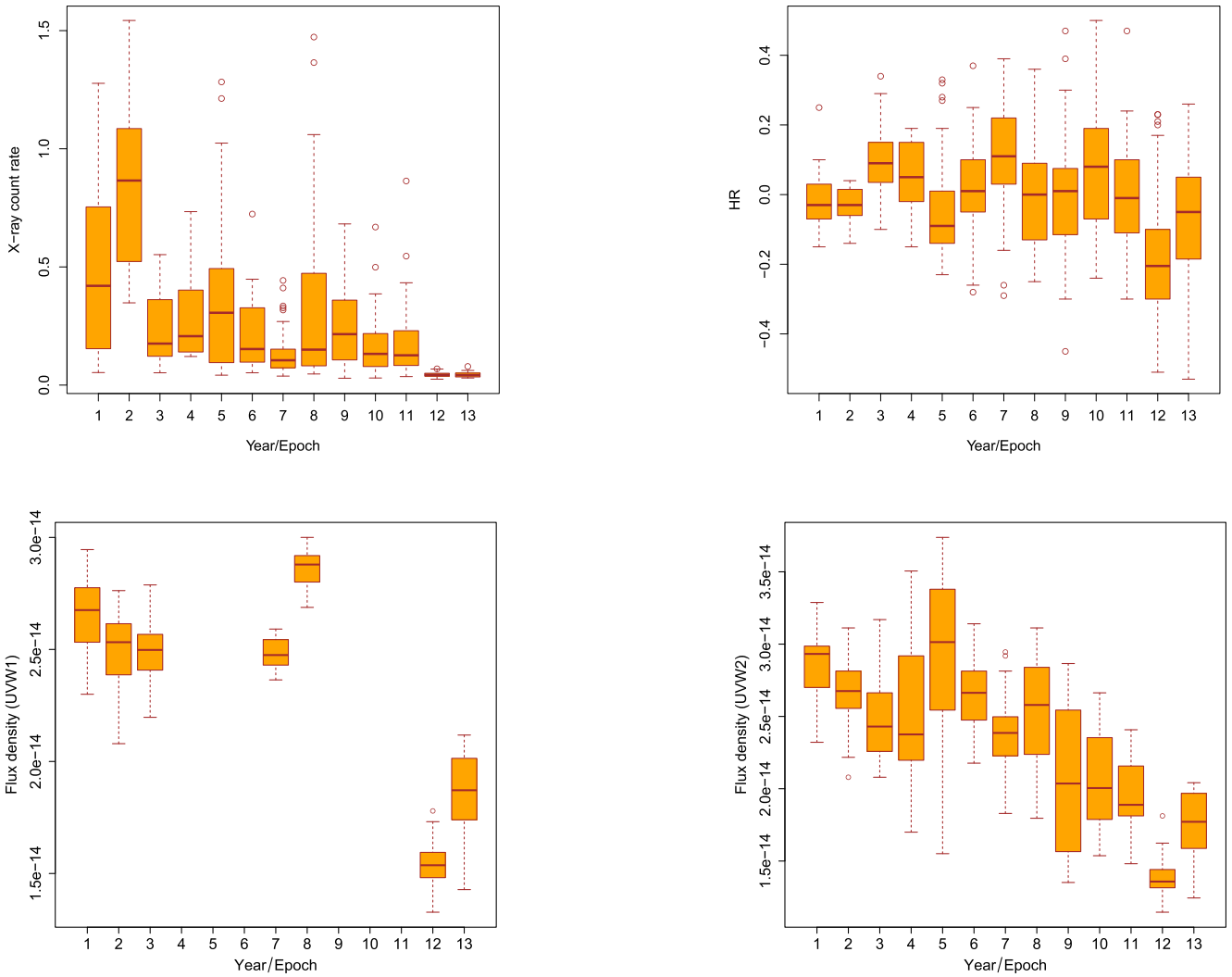

Figure 4. Boxplots of various parameters to examine the degree of variability during a year. The width of the box describes the variations or spread in the values of any parameter. The brown horizontal line that divides the box into two parts marks the median value. The ends of the box show the upper and lower quartiles. The dashed vertical lines are whiskers that connect to the highest and lowest value of the parameter excluding the outliers shown as open circles. Top panels: Variability in the X-ray count rate and the hardness ratio at each epoch. Bottom panels: Variations of flux densities (in units of erg cm^{-2} s^{-1} $Å^{-1}$) in UVW1 (∼2600 Å) and UVW2 (∼1928 Å) for each epoch. There are no observations in the UVW1 filter for Year 4, Year 6, Year 10, and Year 11. Also, Year 5 and Year 9 are removed due to limited statistics in UVW1.

additional flattening during Year 13 (Fig. 3). F_{uv} and F_{opt} trace a general downward trend with time. Note the significant down step in these values for the recent 2–3 yr.

To show the spread of parameter values within each year as well as year-to-year variations, it is more informative to employ the boxplot diagrams[3] that show the range of possible values for a parameter as well as its median value. Fig. 4 (bottom panel) represent the boxplots of the flux densities corresponding to the UVW1 and UVW2 filters. These diagrams suggest that Mrk 335 has become fainter over the last decade with respect to median values (marked by horizontal brown lines in the boxes). Year 12 shows smaller median and variance values, however for Year 13, the AGN is getting slightly brighter and more variable.

[3]Boxplot displays variation in the data without making any assumptions of the underlying statistical distribution.

4 X-RAY VARIABILITY: MEASURED PARAMETERS

As a first step, we used the 13-yr monitoring data (Table 3), to show the X-ray variability pattern of count rates (CR) and the hardness (HR) parameter through boxplot diagrams (top panel: Fig. 4). Besides the year-to-year variations, boxplot for the X-ray CR again emphasize that Mrk 335 has fallen inactive over the last 2 yr. HR boxplot conveys spectral variability over years. However, there is a small caution to exercise in the interpretation of the HR boxplot. When we take a look at the last 2 yr, it suggests that Mrk 335 was highly variable in the spectra. However, for these years, the count rate was quite low and the HR was based on fewer counts compared to previous epochs.

The second step is to perform the spectral analysis to measure the X-ray parameters. The underlying idea is to examine the general shape of the broad-band continuum by simply fitting with a black-body and a power law. To fit the spectrum of Mrk 335 properly, we would need to include warm absorbers/emission; blurred reflection

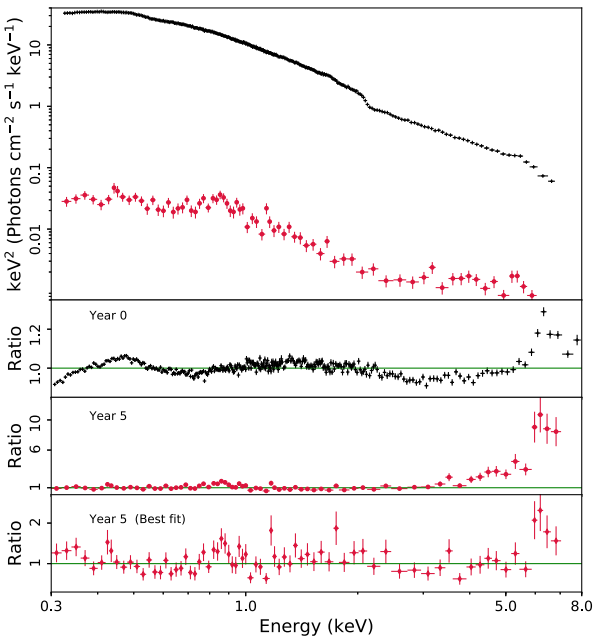

Figure 5. Upper panel: The average X-ray spectrum of Mrk 335 in the pre-2007 bright state (black, crosses) and in one of the low states (Year 5) (red, circles). Spectrum using *XMM–Newton* deep observation in 2006 has been used to represent the pre-2007 bright state. Upper middle panel shows the ratio plot for pre-2007 bright state by fitting the blackbody and power law (black, crosses). Lower middle panel shows the ratio plot using the same pre-2007 model but renormalized to Year 5 (red, circles) and the lower panel shows the best-fitting ratio plot of Year 5 (red, diamonds).

and/or partial covering (e.g. Longinotti et al. 2007; O'Neill et al. 2007; Parker et al. 2014; Gallo et al. 2015). To address the general shape of the spectrum, all the *Swift* XRT spectra during the low state between Year 1 and Year 13 are modelled with a power law and a blackbody with absorption fixed to the Galactic value (Willingale et al. 2013) in the energy band 0.3–10 keV. This model fits all the XRT spectra sufficiently well.

Fig. 5 shows the average high- and low-flux spectrum for Years 0 and 5 along with the ratio plots in the bottom panels. A more detailed modelling of these residuals is out of the scope of this paper and would not provide further insights on the physical origin of these features.

From the spectral modelling of the yearly-averaged X-ray observations, we have computed model parameters and the hardness ratios (Table 7). All the uncertainties presented in the tables and figures correspond to 1σ error bars. The variability of these measured X-ray parameters as a function of time are shown in Fig. 6. The photon index or the spectral shape changes with time, complying with an overall downward trend with scatter; steeper values for the initial epochs, with subsequent flatter values in the later epochs. The blackbody temperature is significantly higher for the Years 12 and 13 when compared to other epochs. Hardness ratios were calculated from the annual spectra using the 0.3–1.0 keV for the soft band and 1.0–10 keV for the hard band, to optimize S/N. For consistency, we have checked that the trend of hardness ratios with time do not change if the soft and hard energy bands are defined as 0.3–2 and 3–10 keV, respectively. In few instances, Year 2 stands out from the other low-flux epochs possibly due to changes in the underlying physical processes.

In addition to measuring the spectral parameters, at each epoch, we also quantify the fractional variability $F_{\rm var}$, soft excess (SE) strength and the optical-to-X-ray spectral slope $\alpha_{\rm ox}$.

A fractional variability analysis ($F_{\rm var}$) determining the relative strengths of observed variability across the energy band has been computed for each year. The yearly variation of the $F_{\rm var}$ computed in the 0.3–10 keV is represented (left, Fig. 7). $F_{\rm var}$ values vary within 70 per cent for all years except for Year 8 where it records fractional variability of 114 per cent. Year 8 is marked by the high X-ray flaring event studied in detail through deep observations (Wilkins & Gallo 2015), and shows the value of $F_{\rm var}$ significantly higher than the average value.

Soft excess is determined from the ratio of blackbody and power-law fluxes computed using the convolution model 'cflux' (within XSPEC `v12.9.1`) in the energy band 0.3–1.0 keV for all the years. The time variability of soft excess shows a gradual downward trend (right, Fig. 7). This shows that the source is consistently exhibiting lesser contribution from the soft X-ray band (0.3–1.0) over the years.

The availability of simultaneous X-ray and UV measurements allow us to gauge the broad-band spectral variability through parameter α_{ox}. It is a hypothetical power law between 2500 Å and 2 keV (Tananbaum et al. 1979) measured from the simultaneous X-ray and UV observations. We find that $\alpha_{\rm ox}$ takes steeper values in general during the low-flux extended period indicating that the X-rays have dimmed more than the UV (left, Fig. 8).

Given the UV luminosity of Mrk 335 measurements of $\alpha_{\rm ox}$ were compared to the expected values (e.g. Strateva et al. 2005). This gives us with a measure of $\Delta\alpha_{\rm ox}(\Delta\alpha_{\rm ox} = \alpha_{\rm ox} - \alpha_{\rm ox}(L_{2500\,\text{Å}}))$ and is an indicator of the X-ray strength compared to the UV.

Mrk 335 displays values of $\Delta\alpha_{\rm ox} \approx 0$ during the bright state, indicating that it appears like a typical or 'normal' AGN. It is interesting to note that during the low extended period despite large uncertainties, the source show nearly constant behaviour, at least, for a few epochs, suggesting a new 'normal' state. Physically, it might imply that after acquiring the X-ray dim state, X-rays and UV both are possibly varying in similar strength for those epochs as shown in Fig. 8.

5 SPECTRAL ENERGY DISTRIBUTION: ANALYSIS AND MEASUREMENTS

In this work, the SEDs of Mrk 335 over the 13-yr *Swift* monitoring period are constructed with the simultaneous multiwavelength optical/UV to X-ray data. The X-ray emission gives valuable insight into the processes in the innermost regions of the supermassive black hole, while the UV radiation emanating from the accretion disc dominates the bolometric emission. Therefore, studying the simultaneous broad-band SED of Mrk 335 makes it possible to investigate the link between the accretion disc and corona. For the preparation of SEDs, we have made use of the *Swift* XRT, UVOT data and the optical spectra (from other instruments), if available. Also, the number of observations of Mrk 335 by *Swift* over the 13-yr period provide an opportunity to study the variation of these SEDs in a systematic manner. In addition, we have made average, flux-resolved SEDs on which the analysis and measurements were performed as described in the following subsections.

5.1 The 13-yr average dim SED compared to the bright state SED prior to 2007

The SED of Mrk 335 in the bright state and the 13-yr average dim state are constructed using the simultaneous optical–UV to X-ray data with *Swift* as shown in Fig. 9.

First of all, we plotted the simultaneous optical/UV and X-ray data in the keV–νL_ν rest-frame plane for each year/epoch (First panel, Fig. 9). To facilitate the computation of SED, we have employed

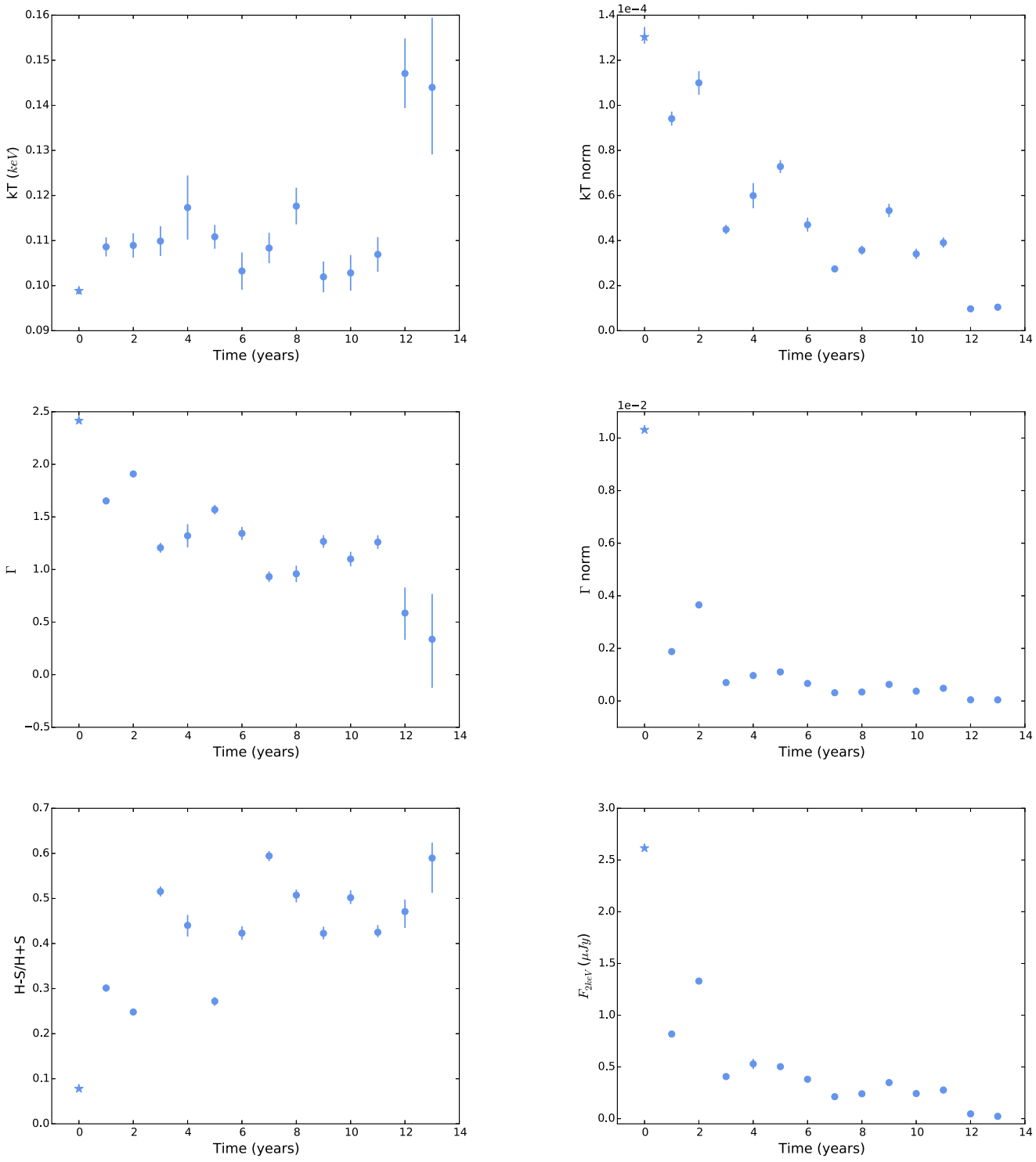

Figure 6. Top panel (left to right): Variations of blackbody parameters (kT and $kT_{\rm norm}$). Middle panel (left to right): Power-law parameters (Γ and $\Gamma_{\rm norm}$). Bottom panel: Hardness ratio and flux density at 2 keV with respect to time. Year 0 represents bright state of Mrk 335 and is represented by a 'star' symbol. $kT_{\rm norm}$ is in units of $(R_{\rm in}/{\rm km})/(D/10\ {\rm kpc})$, where $R_{\rm in}$ is the inner radius and D is the distance and $\Gamma_{\rm norm}$ is in units of photons keV^{-1} cm^{-2} s^{-1} at 1 keV.

an empirical SED template generated for the low-luminosity AGNs in the SDSS-DR7 catalogue in a recent study by Krawczyk et al. (2013).

Krawczyk et al. 2013 studied the SEDs for 119 652 AGNs using mid-infrared (mid-IR) data from *Spitzer* and *WISE*, near-infrared data from the Two Micron All Sky Survey and UKIDSS, optical data from the Sloan Digital Sky Survey, and UV data from *GALEX*. Regarding our work, we have used the mean SED for low-luminosity AGNs ($\log(\nu L_\nu)|_{\lambda=2500\ \text{Å}} \leq 45.41$). We will refer to this SED template as 'Krawczyk model' in the remainder of this paper.

We performed the measurement of SED by splitting the data into three parts. In the first part, we consider data that roughly spans

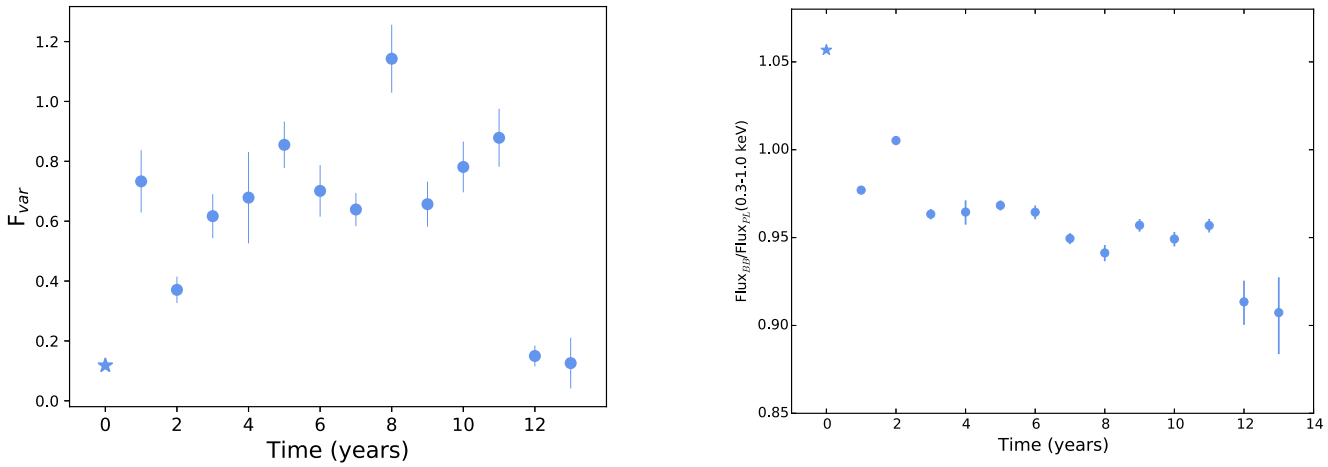

Figure 7. Left: Fractional variability over time. Right: Soft excess determined from the ratio of fluxes computed with 'cflux' in 0.3–1 keV for the model component blackbody and power law. Year 0 represents high state of Mrk 335 and is represented by a 'star' symbol.

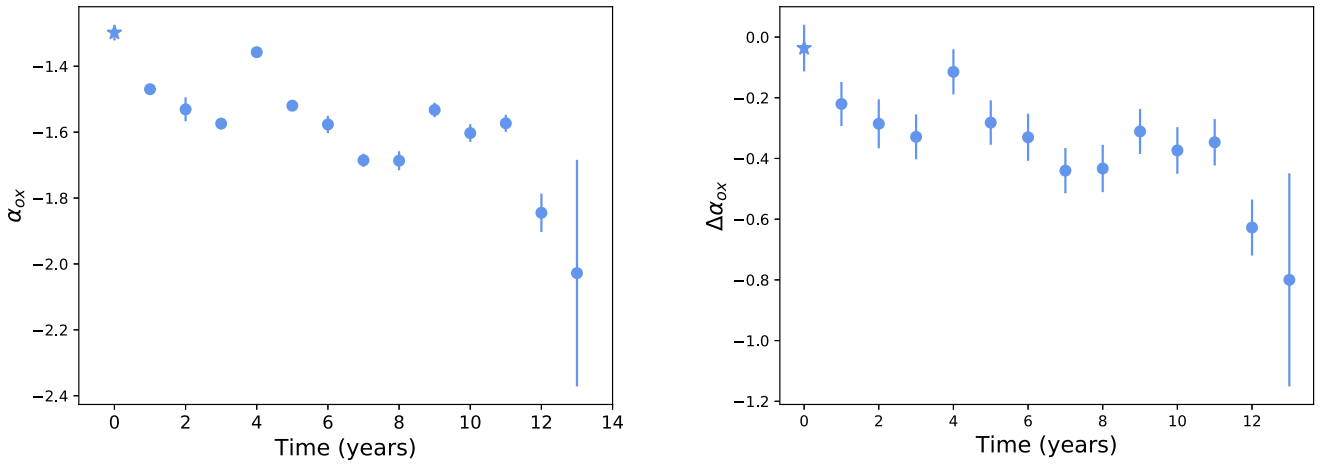

Figure 8. Left: The time variability of the optical-to-X-ray spectral slope α_{ox} is shown. Right: Variation of $\Delta\alpha_{ox}$ with time. Year 0 represents high state of Mrk 335 and is represented by a 'star' symbol.

the frequencies between 1 μm−912 Å. Then the Krawczyk model is used for the data that covers the frequencies between ∼1 μm−912 Å. The Krawczyk model was not extended for the frequencies in the X-rays as their measurements were done through extrapolation on limited X-ray data while we have the available simultaneous X-ray data to make reliable estimates. The full Krawczyk model on the bright state data are plotted [second panel (upper, right), Fig. 9]. Now, Krawczyk model is modified for the data at normalization wavelengths of 2500 and 5100 Å. This is simply done by scaling the Krawczyk SED template with the ratio of rest-frame luminosity (νL_ν) point at 2500 Å in our data and Krawczyk model $\frac{\nu L_{\nu(\rm data)}}{\nu L_{\nu(\rm model)}}$. Similar calculation was performed to modify the Krawczyk model at the normalization wavelength 5100 Å.

In the second part, we need to extrapolate the data in the UV to X-ray gap (912 Å−0.3 keV) to compute the bolometric luminosity. In each SED, we assume a power-law spectrum to the modified Krawczyk model at its rest-frame νL_ν point at 912 Å. We then linearly connect this luminosity at 912 Å to the luminosity corresponding to the frequency of 0.3 keV.

$$L_\nu = (L_{1\,\rm keV}) \times (\nu/1\,\rm keV)^b, \quad (2)$$

where b is the spectral index of the extreme UV region.

For the third part spanning the X-ray data, we deduced the total unabsorbed luminosity through spectral modelling between the energy range 0.3–2 keV only. The data beyond 2 keV has not been used to avoid the double counting of photons resulting due to reprocessing processes (Krawczyk et al. 2013). Finally, the bolometric luminosities are computed for each year/epoch by integrating[4] luminosities from three parts in the keV–νL_ν rest-frame plane as discussed above.

The measured bolometric luminosities for the bright and 13-yr average dim states are $L_{\rm Bol} = 5.53 \times 10^{44}$ and 2.43×10^{44} erg s^{-1}, respectively.

5.2 Flux-resolved SED

To perform the flux-resolved SED analysis, first the X-ray count rates in the soft band (0.3–1 keV) and the hard band (1–10 keV) were calculated using the hardness ratios. These count rates were sorted into four flux intervals defined as high, mid-high, mid-intermediate,

[4]PYTHON package ('simps') was used to perform integration.

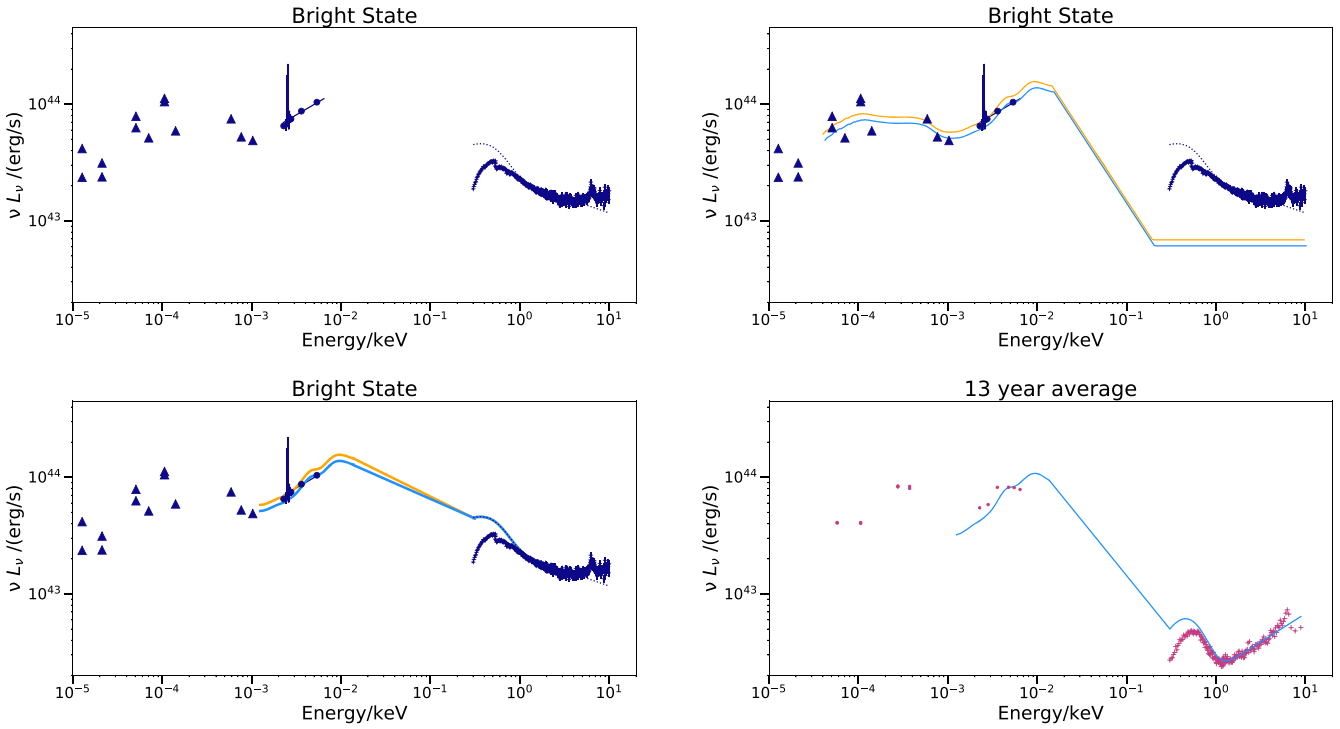

Figure 9. First panel (upper, left): Shows data for the bright state of Mrk 335. Archival infrared data represented in triangles are shown for visual purpose only. Dotted line depicts the unabsorbed model over the X-ray data and the solid line connecting the UV data defines the spectral slope α_{UV}. Second panel (upper, right): Shows the Krawczyk model (derived for the low-luminosity quasars in the SDSS-DR7 catalogue in Krawczyk et al. (2013)) by solid lines in blue and yellow corresponding to 2500 and 5100 Å normalizations, respectively, in addition to the data for bright state. This empirical model spans the mid-infrared (1 μm) to the far ultraviolet FUV (912 Å) region in the rest frame. It is clear that the template does not accurately predict the X-ray emission in Mrk 335. Third panel (lower, left): Shows the modified Krawczyk SED model as described in this work. Specifically, the 1 μm–912 Å SED is connected via a power law to the unabsorbed X-ray spectrum at 0.3 keV. Fourth panel (lower, right): Similar to the third panel, but for the 13-yr average. Only the model normalized to 2500 Å is shown for clarity. Also, notice the steepness of the power law connecting the point at 912 Å and the point at ∼0.3 keV from the bright state to 13-yr average SED of the source.

Table 8. Variations of the X-ray spectral parameters over flux epochs.

Flux-epoch	kT (eV)	$kT_{\rm norm}$[a]	Γ	$\Gamma_{\rm norm}$[b]
High	109 ± 3	1.42 ± 0.07	1.95 ± 0.03	4.40 ± 0.12
Mid-high	110 ± 2.7	1.18 ± 0.06	1.85 ± 0.03	3.12 ± 0.10
Mid-low	105 ± 1.6	0.84 ± 0.01	1.53 ± 0.02	1.42 ± 0.03
Low	114 ± 1.6	0.26 ± 0.01	0.91 ± 0.03	0.26 ± 0.01

[a] $kT_{\rm norm}$ is in units of 10^{-4} ($R_{\rm in}$/km)/(D/10 kpc), where $R_{\rm in}$ is the inner radius and D is the distance.
[b] $\Gamma_{\rm norm}$ is in units of 10^{-3} photons keV^{-1} cm^{-2} s^{-1} at 1 keV.

and low flux represented by horizontal dashed lines in the top plot of Fig. 10. Subsequently, the data corresponding to these four intervals are plotted in the SED diagram along with the corresponding UVOT data in the keV–νL_ν rest-frame plane. These are multiplicatively scaled with the yearly SED model template using the same procedure as described in Section 5.1 and then integration is performed to yield the corresponding bolometric luminosities (Fig. 11). The bolometric luminosities computed for the four intervals, i.e. high, mid-high, mid-low, and low flux are $L_{\rm Bol} = 3.83 \times 10^{44}$, 3.51×10^{44}, 3.09×10^{44}, and 2.00×10^{44} erg s^{-1}, respectively.

X-ray spectral analysis were also performed for these flux intervals and the measured spectral parameters are presented in Table 8.

5.3 Year-averaged SED

The individual yearly SEDs are generated using the same procedure described in the Section 5.1. For comparison, the SEDs were normalized at 2500 and 5100 Å. Both produced comparable results. These models were then used to compute the bolometric luminosity $L_{\rm Bol}$ each year. These SEDs are compiled in the Appendix A. For Years 0, 4, 8, 9, 10, and 12, the optical spectroscopic data were available to include in the SEDs.

$L_{\rm Bol}$ is often divided by $L_{\rm Edd}$ to yield a parameter that is proportional to the accretion rate, which is generally called as Eddington ratio and commonly described by the symbol $\lambda = L_{\rm Bol}/L_{\rm Edd}$, where $L_{\rm Edd}$[5] is the maximal theoretical luminosity to account for the equilibrium between the radiation pressure and the gravitational force.

The variation of the SED models of Mrk 335 for all the years with respect to normalization wavelength at 2500 Å are shown in Fig. 12.

We have measured the yearly variability of bolometric luminosity Eddington ratio $L_{\rm Bol}/L_{\rm Edd}$ (decrease at 11 per cent level) and the X-ray to bolometric luminosity ratio $L_{\rm x}/L_{\rm Bol}$ (decrease at 4 per cent level) in Fig. 13. $L_{\rm Bol}/L_{\rm Edd}$ follow a significant downward trend from the pre-2007 epoch to the low state epochs.

[5] $L_{\rm Edd} = 1.26 \times 10^{38}$ ($M_{\rm BH}$/M$_\odot$) erg s^{-1}, where M$_\odot$ is the mass of the Sun.

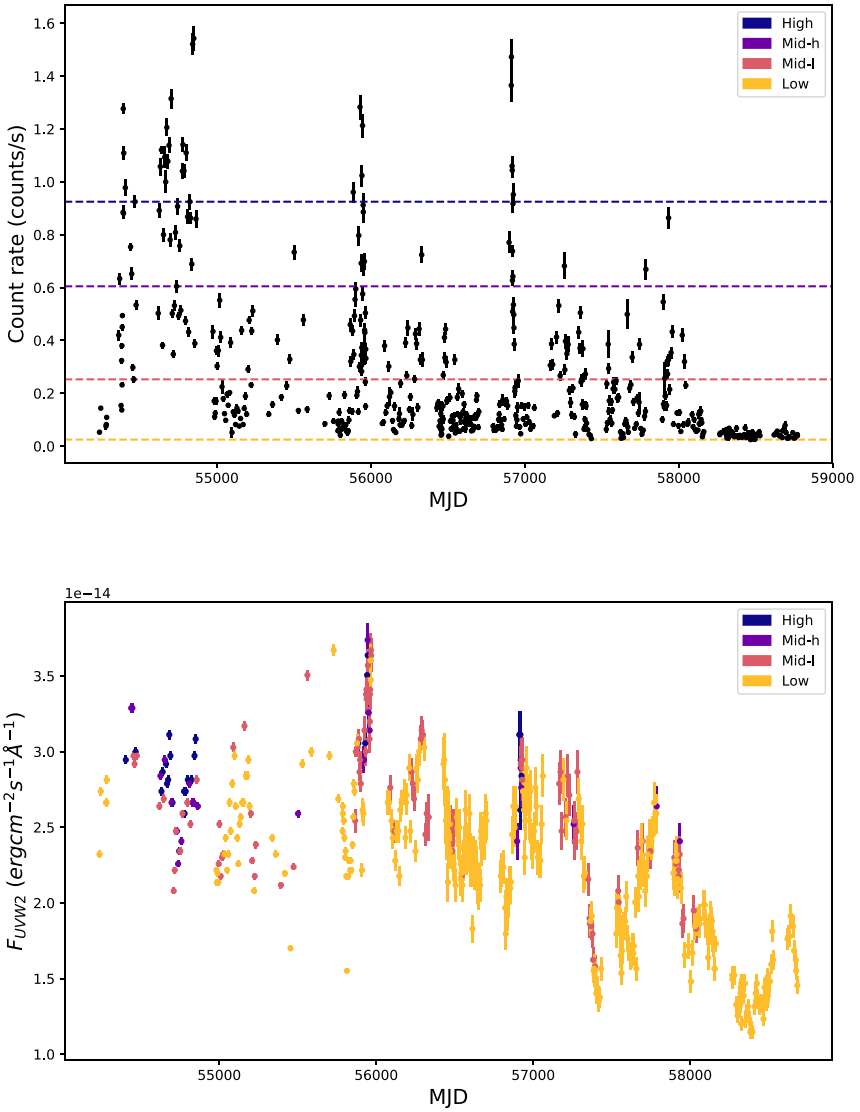

Figure 10. Top to bottom: X-ray light curve of Mrk 335. The cuts in the count rates are shown as horizontal lines whereas the UVOT light curve is colour-coded, defined by the X-ray flux cuts.

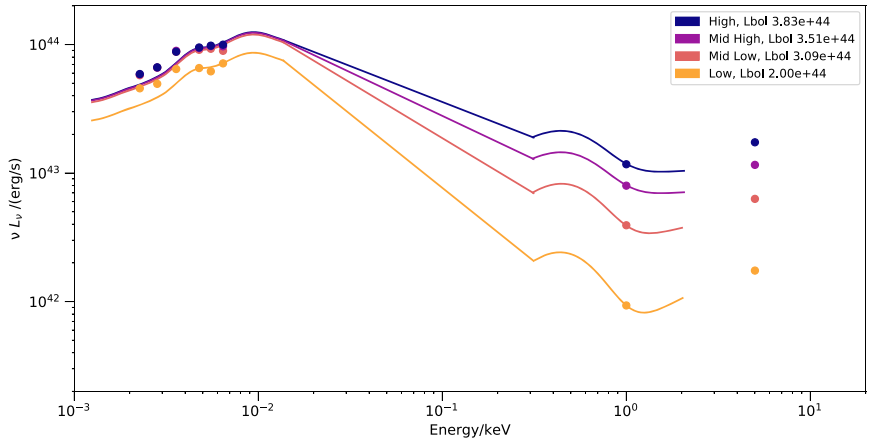

Figure 11. SED plot for the flux-resolved data of Mrk 335.

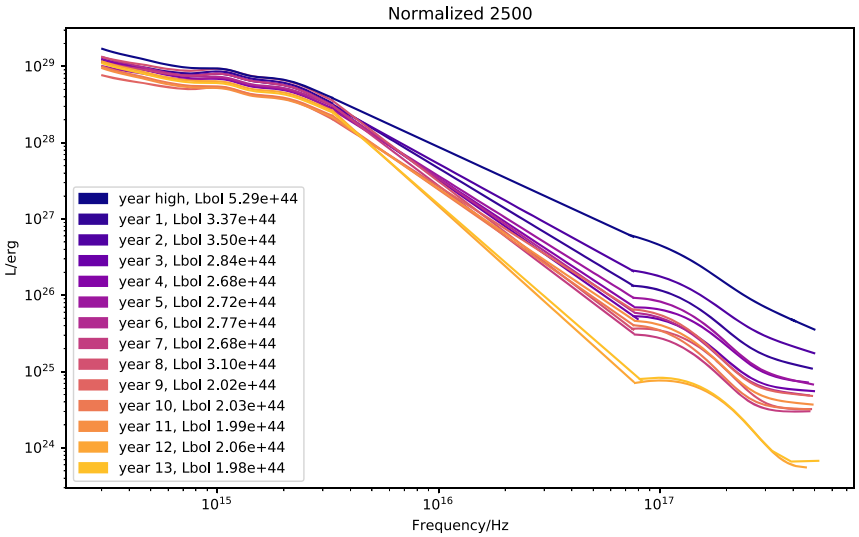

Figure 12. SED measurements for all years with normalization at 2500 Å.

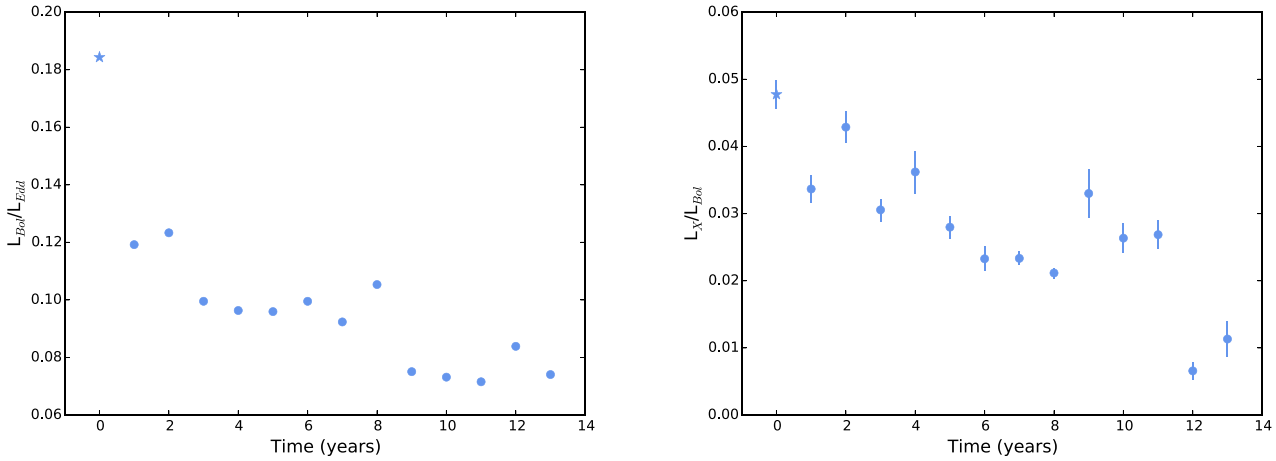

Figure 13. From left to right: Bolometric luminosity Eddington ratio with time and the X-ray to bolometric luminosity ratio, assuming the black hole mass of $(25 \pm 3) \times 10^6$ $M_\odot$ (Grier et al. 2012). Year 0 represents bright state of Mrk 335 and is represented by a 'star' symbol.

6 INVESTIGATING CORRELATIONS BETWEEN THE SED PARAMETERS

6.1 Correlation analysis

We have searched for the correlations among the measured parameters. To present the results of the correlation analysis in one plot, a correlation matrix function 'corrplot' (Wei & Simko 2017) in 'R' (R Core Team 2013) is used as shown in Fig. 14. This correlogram is used here to highlight the most correlated variables in Table 7. We have excluded the flux density at 2 keV from the analysis as by definition, this parameter is redundant with α_{ox}. The colours (as well as the orientation) of ellipses in the correlogram show positive or negative correlations while the width of the ellipses implies the strength of correlation. We discuss the important findings of this analysis below.

The blackbody temperature (kT) (i.e. the shape of the soft excess) and the hardness ratio (HR) show a moderate correlation with time (i.e. year). There is no obvious relation between time and either F_{varUV} or F_{var}. All other parameters show an anticorrelation with the time.

The soft excess emission (SE) shows significant correlations with several parameters. We find a very strong correlation between the soft excess and L_x/L_{Bol}. This could be due to the contribution of primary X-ray emission in the soft excess strength, as defined in our work. Some studies have indicated that the lack of inverse correlation between the soft excess and 2–10 keV L_x/L_{Bol} could possibly disfavour the reflection and absorption scenarios, and could be naturally explained by the warm Comptonization scenario (e.g. Gliozzi & Williams 2020). There is a clear correlation between the soft excess and the steepness of the X-ray spectrum (Γ), however, we found only a marginal relationship with L_{Bol}/L_{Edd}. Some studies have found that L_{Bol}/L_{Edd} is positively correlated to soft excess emission (SE; e.g. Boissay, Ricci & Paltani 2016). Both the soft excess and L_x/L_{Bol} are correlated with α_{ox} indicating as the X-ray brightens so to must the UV. Interestingly, there is also a tight correlation between SE and α_{uv} possibly suggesting a common mechanism in the soft X-ray and UV bands.

The parameter L_{Bol}/L_{Edd} is significantly correlated with time, implying a decrease in its strength successively each year. L_{Bol}/L_{Edd}

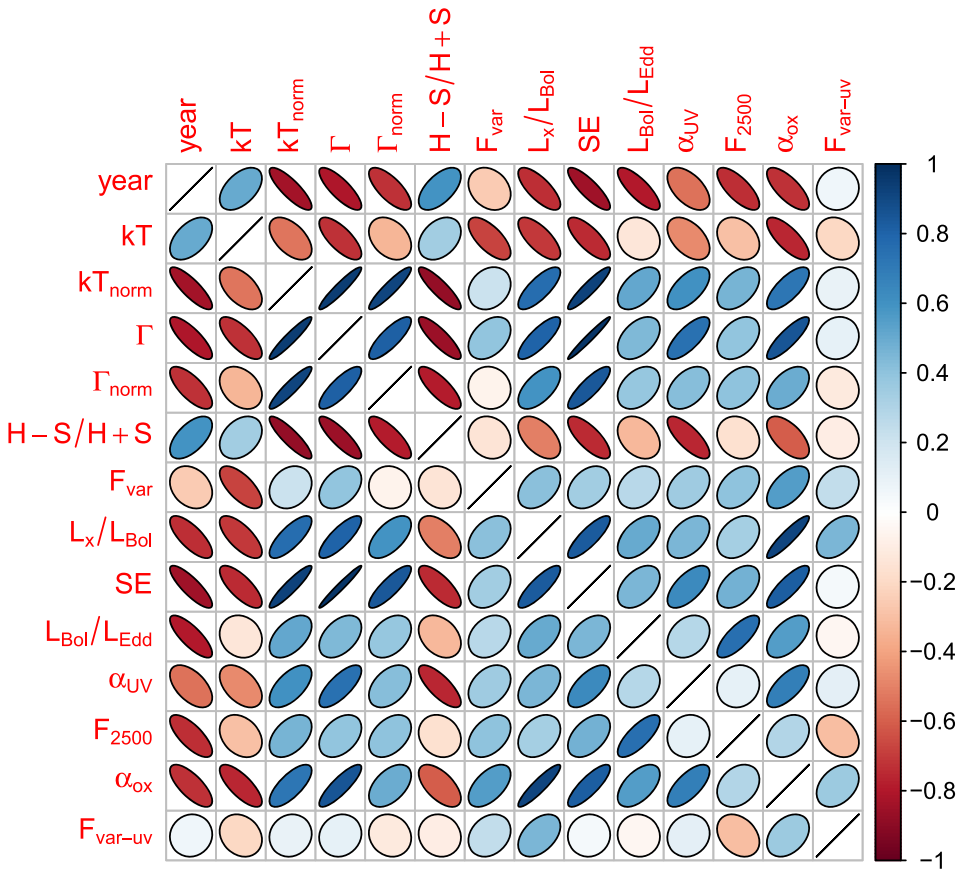

Figure 14. Correlogram shows all the correlations among the variables presented in Table 7. Correlation coefficients is coloured according to the value such that the colours of the ellipse indicate the sign of the correlation, and their shapes indicate the strength (narrower ellipses = higher correlations).

shows weak correlation with photon index Γ. This dependance has been studied for Mrk 335 in the previous works (e.g. Sarma et al. 2015; Keek & Ballantyne 2016) and a positive correlation has been found in the previous studies on large samples that have shown that $L_{\rm Bol}/L_{\rm Edd}$ is indeed the primary parameter driving the conditions in the corona, giving rise to Γ (e.g. Grupe 2004; Porquet et al. 2004; Wang, Watarai & Mineshige 2004; Bian 2005; Shemmer et al. 2006, 2008; Kelly et al. 2007; Risaliti, Young & Elvis 2009; Jin, Ward & Done 2012; Brightman et al. 2013; Fanali et al. 2013; Gliozzi & Williams 2020). The weaker correlation found in this work possibly suggest that we may not be necessarily measuring the true shape of the power law since the spectrum is modified by absorption or reflection that we do not include. $L_{\rm Bol}/L_{\rm Edd}$ appears only moderately correlated with X-ray normalization parameter of blackbody ($kT_{\rm norm}$) and $L_{\rm x}/L_{\rm Bol}$.

An interesting significant correlation is found between $L_{\rm Bol}/L_{\rm Edd}$ and F_{2500}. This is rather a surprising result as F_{2500} is not found to be correlated with any other parameter except with year. Statistically, this correlation could be driven due to their strong dependance on time. Otherwise, physically, it could suggest the possible influence of conditions driving the changes in the accretion rate on 2500 Å emission.

$L_{\rm Bol}/L_{\rm Edd}$ is seen to be positively correlated to $\alpha_{\rm ox}$ which is in consistence with the previous studies on the sample of luminous AGNs ($L_{\rm Bol}/L_{\rm Edd} > 10^{-3}$ to 10^{-2}) that have derived this positive relationship with the slope of such as 0.397 (Lusso et al. 2010), and 0.11 (Grupe et al. 2010). This is interesting as we did not find any correlation between $\alpha_{\rm ox}$ and F_{2500} and this could probably mean that the Eddington ratio (or accretion rate) is possibly playing role in driving the changes in the X-ray strength. Previous studies on the optically selected samples and X-ray samples have found strong dependance between $\alpha_{\rm ox}$ and L_{2500} (e.g. Vignali, Brandt & Schneider 2003; Strateva et al. 2005; Lusso et al. 2010).

Next, concentrating on $L_{\rm x}/L_{\rm Bol}$, it is positively correlated with the photon index Γ, blackbody parameters and $\alpha_{\rm ox}$. For high-redshift sources, the positive dependance of Γ with X-ray luminosity has been noted (e.g. Dai et al. 2004; Saez et al. 2008) but not observed in the sample of local AGN (e.g. Brightman et al. 2013).

We checked the correlations of $F_{\rm varUV}$ and $F_{\rm var}$ with all the parameters. $F_{\rm varUV}$ is not correlated with any parameter. However, we find some interesting behaviour from the parameter $F_{\rm var}$. During the 13-yr low state, it is found to be significantly anticorrelated with blackbody temperature (kT) and positively correlated with $\alpha_{\rm ox}$; however, the correlations disappear if the bright state (Year 0) is included in the analysis. This suggests an important result that the 13-yr monitoring period has been witnessing significant X-ray variability in the source although being in an X-ray low state. Also, if kT can be assumed to indicate the ionization of the absorbing or reflecting material, the anticorrelation between $F_{\rm var}$ and kT might suggest the amplitude of the variations diminish when the ionization is high.

One of the many interesting results that arise from this analysis is that overall behaviours in an individual AGN, i.e. Mrk 335, mirror the range of variations and their correlations as seen in large samples of different objects. Perhaps this suggest that the same physical process applies in all cases, and is scalable in some form. The physical

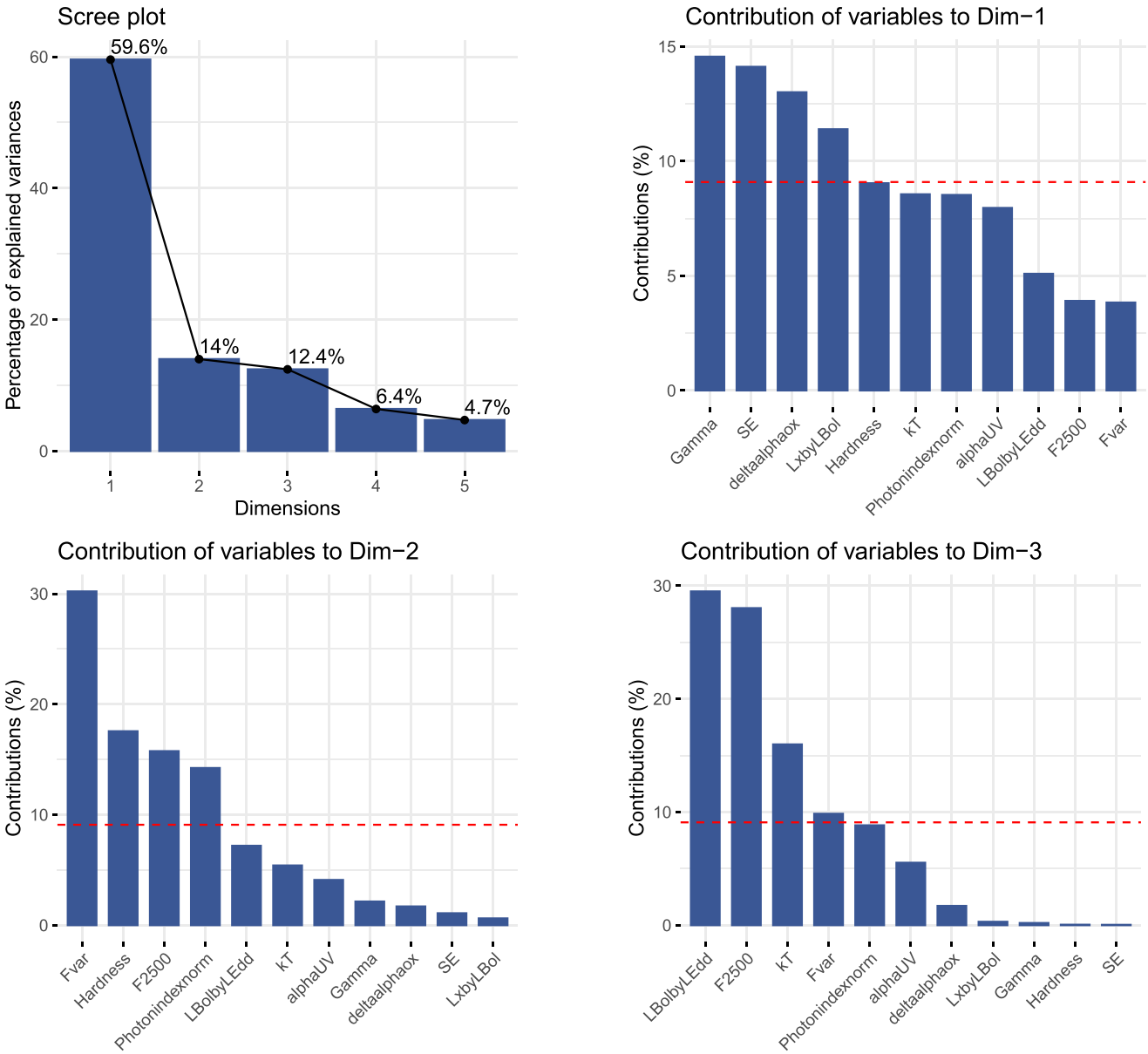

Figure 15. Upper left: shows the screeplot from the PCA on all the parameters presented in Table 7 which is the plot of eigenvalues ordered from largest to the smallest. The number of components are determined at the point, beyond which the remaining eigenvalues are all relatively small and of comparable size, Upper right figure shows the bar plot of contributions from all the variables to principal component 1. The red dashed line on the graph above indicates the average of contribution from all the parameters. Figures on the lower left and lower right represent the bar plots of contributions of variables to principal components 2 and 3, respectively.

scenarios that can predict/produce these relationships are discussed in detail in Section 7.

6.2 Principal component analysis

PCA (Francis & Wills 1999) is a statistical method to determine relevant properties that explain the maximum amount of variability in the data set. It is often useful to visualize complicated processes involving multiple physical parameters through PCA analysis. We performed PCA using function 'FactoMineR' (Lê, Josse & Husson 2008) in 'R' on the multiwavelength data of Mrk 335 presented in Table 7, and the results are shown in Fig. 15. We have excluded few parameters such as $F_{2\,\mathrm{kev}}$, F_{varUV} (uncorrelated with parameters) and kT_{norm} (redundant with SE) from the analysis. This is necessary to eliminate noise in the PCA output from the uncorrelated/redundant variables. Also, α_{ox} is replaced with $\Delta\alpha_{\mathrm{ox}}$. An important point to note is that we have carried out this analysis on the parameters for the low extended 13-yr period (Table 7, Years 1–13) in order to investigate the underlying cause of variability within the monitoring data.

The first step in the PCA analysis is to determine the number of significant principal components in the data. This is done by generating a screeplot (upper left, Fig. 15) that plots the variances (inpercentages) against the number of the principal component. With our data set, this resulted in the three significant principal components that cumulatively account for ∼86 per cent of variance in the data. Next step is to investigate these principal components

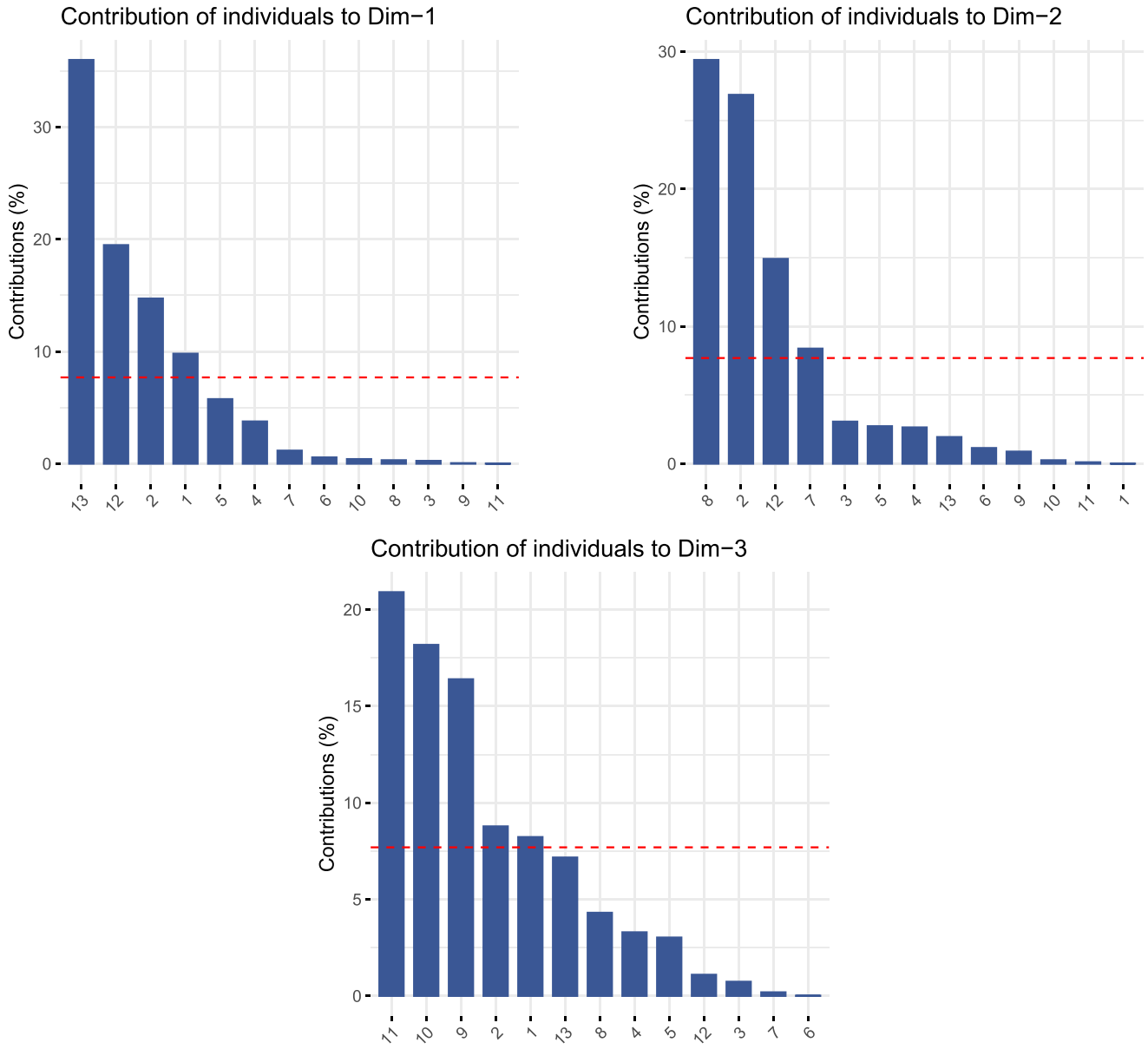

Figure 16. Upper Left: shows the contribution of individual years to the first principal component. The red dashed line is the reference line corresponding to the expected value if the contributions were uniform. The upper right and lower panels shows the specific years significantly contributing to the second and third principal components, respectively.

and get information on the set of parameters that give rise to each one of them.

It is interesting to see that the first principal component has the most significant contributions (above the marked line in 'red') from the X-ray parameters, i.e. photon index Γ, soft excess (SE), X-ray weakness ($\Delta\alpha_{ox}$), and normalized X-ray luminosity (L_x/L_{Bol}). The data are well described by this principal component which accounts for more than ∼60 per cent variability (upper left, Fig. 15) through the X-ray parameters.

The second principal component accounting for ∼14 per cent of the variability is further influenced by the X-ray parameters. The most important parameters here are the fractional variability (F_{var}) (∼30 per cent), hardness ratio (18 per cent). F_{2500} and photon index normalization (Γ_{norm}) have marginal contributions (15 per cent).

The third principal component is driven significantly (∼30 per cent equal contribution) by L_{Bol}/L_{Edd} and the optical–UV parameter F_{2500}. This principal component carries about ∼12 per cent variability of the data.

The fourth principal component has marginal contribution (∼6 per cent) to explain the variability of data through ultraviolet parameter alone (α_{uv}).

This analysis is a statistical, model-independent approach to understand the significance of the multitude of parameters describing the data set in terms of variability. However, it is subject to limitations in terms of physical meaning to the outcomes of this analysis. The analysis suggests clearly the dominance of X-ray properties of the source towards the primary variability (∼70 per cent), as also suggested by correlation analysis. Less impor-

tant are the changes in the optical–UV properties of the AGN (∼8–10 per cent).

In order to further explore the role of years or epochs that possibly drive these principal components, we made the contribution plots as shown in the Fig. 16. The first plot (upper right) reveals the individual years that highly contributed towards the variability exhibited by the PC1. Year 13, Year 12, Year 2, and Year 1 show the significant contribution to PC1. The second principal component has significant contribution from Year 2 and Year 8 (∼30 per cent). The third principal component reveals the epochs marked as Years 11, 10, and 9 in the order of their contributions. It is interesting to speculate that the most significant X-ray changes occurred in early years (e.g. 1 and 2), but the significant UV changes occur in later year (e.g. 9, 10, and 11). This could be suggesting of a driving mechanism if we believe the X-ray changes could have resulted in later UV changes.

These results can be interpreted such that the most significant variations in the properties of the source seem to have taken place in Years 2, 8, 9, 10, 11, 12, and 13. Some of these epochs have deep observations to help understand the physical driver of variability. For instance, Years 12 and 13 are peculiar as recent observations with *XMM–Newton*/*HST* campaign have suggested the scenario of strong UV absorption (Parker et al. 2019). Year 2 stands out as discussed in Section 4 with respect to its unique X-ray flaring behaviour compared to other epochs (Fig. 6) and also is marked by weaker UV absorption (Longinotti et al. 2013). Year 8 is also the X-ray flaring year attributed to collimated, relativistic outflow that could also produce UV emission (Wilkins & Gallo 2015). It is interesting that Year 9 and Year 10 stood out in PCA results despite excluding $F_{\rm varUV}$ from this analysis. Year 9 have shown maxima similar to Year 4 in Fig. 3 (top, left).

We considered the effect on the PCA results of omitting Years 12 and 13 since the X-ray data were of low counts during these epochs. There was a big change in Years 12 and 13 corresponding to another drop in flux and the source became X-ray weaker compared to previous years. Excluding these years, the PCA then emphasizes the X-ray flaring years (Years 2 and 8) and the UV flaring Year 4. Even though these later years have lower quality X-ray data, their contribution to the 13-yr PCA is still important to include.

7 DISCUSSION

Our study of the SED of Mrk 335 using multiwavelength data has led to the annual estimation of bolometric luminosity and luminosity Eddington ratio. A detailed correlation analysis was performed between the measured X-ray and UV parameters spanning the monitoring period. An interesting finding from our comprehensive correlation study is that nearly all these correlations have been shown in previous studies on different samples of AGN. This is remarkable as it suggests the similar physics at work for an individual source like, Mrk 335 and in other AGNs as well.

An interesting behaviour can be seen for the soft excess emission of Mrk 335 over the monitoring period, which is found to be highly correlated with many parameters. For spectral analysis, we have used a thermal blackbody to model the thermal emission from an optically thick accretion disc to a first-order approximation. Although constraining the temperature of the soft excess using a thermal blackbody is not physically meaningful, it still provides a helpful measurement that can be utilized for comparison with other data. The blackbody kT has weak dependance on the black hole mass, thus, ruling out a thermal origin from the accretion disc. However, invoking the atomic physics could still explain the values taken by kT, for instance, in the context of strong, relativistically blurred absorption from a disc wind (Gierliński & Done 2004), kT will still reflect whether the ionized gas is lowly or highly ionized. Similarly, in the case of blurred ionized reflection which is sensitive to the ionization state of the reflecting material (Crummy et al. 2006), kT could be a useful indicator.

For the 13-yr monitoring data, kT shows variability, more prominently for the last two epochs. This would then imply that there are other additional processes at work. So, it is still a meaningful parameter, but for different reasons other than measuring a disc temperature.

At the same time, it is to be noted that accurate constraints of parameters, e.g. Γ and kT become difficult in the low count statistics regime; at least, such is the case for the past 2 yr with measurements of higher blackbody temperatures (∼140 eV) and flatter photon indices (∼0.6). It is interesting to note that the power-law shape, pertaining to the flatter photon indices, might be indicative of the onset of other processes. Nevertheless, several correlations of soft excess found in our study might give some clues to compare the physical processes weaved into realistic scenarios (e.g. blurred reflection, soft Comptonization).

Blurred reflection model can explain the observed correlation of soft excess with photon index and $F_{\rm var}$. This scenario occasionally implies a strong suppression of the intrinsic power-law continuum to account for a rather pronounced soft excess, as justified in the context of strong light-bending effects (Miniutti & Fabian 2004). An increase in the strength of soft excess emission could arise as a result of an increase in ionization parameter and/or reflection fraction. The overall effect would be a suppressed primary power-law continuum (implying reduced variability) and an enhanced soft excess (i.e. reflected emission) (Crummy et al. 2006). This can naturally predict the observed correlation between soft excess and photon index.

Next, the observed X-ray variability could be driven by the changes in the primary power-law continuum possibly manifested through intrinsic variations in the corona, or possible changes in its size or location throughout the monitoring period. From our analysis, we find $F_{\rm var}$ to be inversely correlated to blackbody temperature and positively correlated to blackbody normalization. This would suggest a suppressed power law thereby, resulting into reduced variability. Such a scenario could possibly mimic the observed correlation between $F_{\rm var}$ and kT.

Alternatively, in the framework of soft Comptonization, we find a tight relationship between the soft excess and the photon index and no inverse correlation with the X-ray luminosity. A part of this enhanced soft excess emission would undergo upscattering by the hot electrons in the corona to produce the primary X-ray power-law continuum. This eventually cools off the corona, and could possibly explain the correlation between the photon index and the soft excess strength (Done et al. 2012). Both these scenarios can explain some of the observed correlations found in this study.

If we take a closer look at the SED analysis, the differences in the SED shape over these 13 yr show a systematic downward trend. Such a systematic downward trend has been investigated on the optical photometric data of Mrk 335 during 1995–2004 by Doroshenko et al. (2005). They found that Mrk 335 exhibit large amplitude variability reaching about 1.1, 0.9, 0.7, 0.3, and 0.3 mag in the U, B, V, R, and I bands, respectively. The brightness was systematically decreasing since 1995 by about a factor of 2.5, and the variations of different amplitudes and duration were suggested. In addition, the shape of the SED remained constant in spite of these flux-variations.

This is quite interesting as the source continued to dim in the optical over a time-scale of 10 yr. The abrupt change in the X-ray brightness occurred after 2 yr of this study, i.e. in 2007. It is

relevant to understand the scenarios that can explain the time-scales of the observed variations in this source over the long term. For the optical emission region, the time-scale for the change in the accretion rate is the viscous time-scale, which by considering the black hole mass of our source and assuming conservative value of disc aspect ratio $h/r \sim 0.01$, should be tens of thousands of years, which is much longer than our current observations. However, time-scales due to local temperature fluctuations, i.e. thermal time-scale can give rise to optical/UV variations on much shorter time-scales (Kelly, Bechtold & Siemiginowska 2009). Despite the different time-scales involved, it might be possible that the abrupt change in the X-ray flux and the more gradual change in the optical emission regions of the source are possibly connected through some process. For instance, Sun et al. (2020) suggest a model which show that the magnetic coupling between the compact corona and the outer cold accretion disc might exist. However, based on the pre-2007 X-ray light curve (e.g. Grupe et al. 2007) that suggests that despite the changes in the optical flux, the source probably stayed relatively normal when compared to α_{ox}. We see that in 2006, after the changes in the optical presumably occurred, Mrk 335 was just a 'normal' AGN.

The present monitoring data however, suggest relatively significant changes ascribed to the UV and X-ray spectral behaviour which is intrinsic to the central engine. The changes in the optical emission are relatively low. During the prolonged low X-ray flux period, the changes in the SED shape are found to be more dramatic for the past 2 yr. Both obscuration and the intrinsic changes linked to either the inner disc or corona could be playing vital roles in Mrk 335, while it exhibits intermittent phases of dimming and flaring over the 13-yr time-scale as indicated by recent studies (Gallo et al. 2019; Longinotti et al. 2019; Parker et al. 2019). Regarding the changes in the inner disc; this could possibly be triggered by disc instabilities, or due to the presence of local perturbers or more distant changes in the accretion flow (Stern et al. 2018).

To investigate the observed long-term X-ray variability, one must consider the changes in the inner accretion disc, where the relevant time-scales are the orbital, thermal, and the viscous time-scales. Gallo et al. (2018) have investigated these time-scales previously in the context of multiband structure functions of Mrk 335. Based on a conservative value of viscosity parameter $\alpha_v \sim 0.1$ and disc aspect ratio $h/r \sim 0.01$ in the standard accretion disc scenario, the characteristic time-scales in the UV and optical wavebands could be attributed to the thermal and orbital time-scales, respectively.

Another important time-scale, i.e. cooling and heating front time-scale due to viscous effects in the accretion disc was not discussed in the previous study, possibly, because this scenario inherently proposes the characteristic time-scales that are too long. In this scenario, a cooling front propagates outward in the disc and reflects back inward as a heating front and has successfully explained the dimming character of few changing look AGNs (e.g. Ross et al. 2018; Stern et al. 2018). As such, these fronts propagate in the disc on time-scales of $t_{\rm front} \sim (h/r)^{-1}\ t_{\rm th}$ where $t_{\rm th}$ is the thermal time-scale. It remains a possibility that a revision of some of these parameters, e.g. α_v might make the cooling/heating front time-scale (Hameury, Viallet & Lasota 2009) relevant in the context of Mrk 335. Considering $\alpha_v \sim 0.4$ and $h/r \sim 0.2$, we find that the $t_{\rm front} \sim 120$ d is consistent with the longer break time-scale which was observed in the 11-yr averaged UVW2 structure function whereas the shorter break time-scale could be explained by the thermal time-scale $t_{\rm th} \sim 24$ d. Also due to the quadratic dependance on h/r, $t_{\rm vis}$ would also drop significantly.

Assuming an albeit higher value of α_v, as found by some studies (e.g. King, Pringle & Livio 2007; Tetarenko et al. 2018), implies more turbulence acting over the neighbouring disc annuli, thereby, leading to an increase in the propagation of fronts and probably resulting in the increased disc emission. Future work with detailed spectral modelling on these data might shed some light on the value of α_v to understand the more plausible time-scale or mechanism in the inner accretion disc.

8 CONCLUSIONS

Mrk 335 was once one of the brightest AGN in X-rays, allowing detailed observations even when it went into its deep low state. We have presented the simultaneous optical-to-X-ray SEDs of Mrk 335 from the 13-yr *Swift* monitoring data. For comparison, the SED for representative bright state of the source is also presented. The SEDs span the infrared, optical, ultraviolet and X-ray regimes ($\approx$1 μm to 2 keV) using a simple empirical model. The X-ray part of the SED is determined separately by incorporating the integrated flux between 0.3 and 2 keV, duly estimated from the simple X-ray spectral model. By employing the 13 epochs of multiwavelength XRT, UVOT photometric and archival optical spectroscopic data, and reverberation mapped mass estimate of Mrk 335, this work presents the following main outcomes:

(i) We see a gradual decreasing trend in the yearly SED models. The most prominent change in the SED is evident during the bright state transition of the source to the extended low-flux period and then during the past 2 yr where a clear dip in the SED model can be noticed.

(ii) Bolometric Eddington luminosity ratio changes significantly over the 13-yr period (full observed range is 0.1–0.07). For the bright state, it is estimated to be ∼0.2.

(iii) Relatively small changes in the optical/UV over 13-yr data are found as compared to more significant changes in the X-ray flux, spectral shape and variability. The total amplitudes of variability observed in UV and X-rays are (∼6–25 per cent) and (∼70–110 per cent), respectively. In fact, when compared to other AGNs, Mrk 335 is still remarkably variable in optical/UV. But relatively rapid and higher amplitude of variability observed in X-rays rather reinforces the preference for structural or intrinsic changes in the corona and/or absorption to explain the observations.

(iv) We tested the utility of these yearly empirical SEDs by measuring the useful parameters in the optical/UV and X-rays, e.g. $L_{\rm Bol}/L_{\rm Edd}, \alpha_{\rm uv}$. We, then performed correlation and statistical analyses on these estimated SED parameters along with the X-ray spectral parameters.

(v) Our comprehensive correlation study yields several significant correlations amongst parameters, most notably, for SE and $L_{\rm Bol}/L_{\rm Edd}$. These relationships have been established in previous studies of other AGNs and therefore suggest that similar physical processes apply, in general, to a majority of AGNs. We found a significant correlation between the soft excess emission and the photon index, but no inverse correlation with X-ray luminosity. This might suggest the possibility of the role of soft Comptonization scenario to explain the long-term X-ray data.

(vi) PCA on this multiwavelength data set reveals higher statistical significance of the X-ray driven variability as compared to the optical/UV variability. The variability shown by PCA are mostly contributed by the X-ray flaring epochs and the recent X-ray dimmest years.

(vii) We have demonstrated that the simultaneous optical–UV and X-ray monitoring data of Mrk 335 continue to provide opportunities for understanding the physical characteristics of this source, particularly, in this work through the determination of SEDs and the statistical analyses. The detailed spectral modelling of these empirical SEDs with regards to the physical scenarios remains an interesting subject for the future work.

ACKNOWLEDGEMENTS

We thank the *Swift* team for approving our various ToO requests to monitor Mrk 335 over the years. Many thanks to the anonymous referee for providing a thorough report that improved the paper. LCG acknowledges financial support from the Natural Sciences and Engineering Research Council of Canada and the Canadian Space Agency. ALL acknowledges support from CONACYT grant CB-2016-01-286316. This work is partially based on observations made with the Galileo 1.22 m telescope of the Asiago Astrophysical Observatory operated by the Department of Physics and Astronomy 'G. Galilei' of the University of Padova. This research makes use of facilities at the Metsähovi Radio Observatory, operated by the Aalto University, Finland. We thank B. M. Peterson for providing the optical data from MDM Observatory, Kitt Peak, Arizona.

DATA AVAILABILITY

The raw X-ray data used in this work are publicly available in the *XMM–Newton* https://www.cosmos.esa.int/web/xmm-newton/xsa and *Swift* https://www.swift.ac.uk/swift_portal/. Optical data used in this work are available upon request by the authors.

REFERENCES

Arnaud K. A., 1996, ASPC, 101, 17
Bian W.-H., 2005, Chin. J. Astron. Astrophys. Suppl., 5, 289
Boissay R., Ricci C., Paltani S., 2016, A&A, 588, A70
Breeveld A. A. et al., 2010, MNRAS, 406, 1687
Brightman M. et al., 2013, MNRAS, 433, 2485
Buisson D. J. K., Lohfink A. M., Alston W. N., Fabian A. C., 2017, MNRAS, 464, 3194
Burrows D. N. et al., 2005, Space Sci. Rev., 120, 165
Cardelli J. A., Clayton G. C., Mathis J. S., 1989, ApJ, 345, 245
Cash W., 1979, ApJ, 228, 939
Crummy J., Fabian A. C., Gallo L., Ross R. R., 2006, MNRAS, 365, 1067
Dai X., Chartas G., Eracleous M., Garmire G. P., 2004, ApJ, 605, 45
Done C., Davis S. W., Jin C., Blaes O., Ward M., 2012, MNRAS, 420, 1848
Doroshenko V. T., Sergeev S. G., Merkulova N. I., Sergeeva E. A., Golubinsky Y. V., 2005, A&A, 437, 87
Edelson R., Turner T. J., Pounds K., Vaughan S., Markowitz A., Marshall H., Dobbie P., Warwick R., 2002, ApJ, 568, 610
Fanali R., Caccianiga A., Severgnini P., Della Ceca R., Marchese E., Carrera F. J., Corral A., Mateos S., 2013, MNRAS, 433, 648
Francis P. J., Wills B. J., 1999, ASPC, 162, 363
Gallo L. C., 2006, MNRAS, 368, 479
Gallo L. C., 2018, Proc. Sci., Revisiting Narrow-Line Seyfert 1 Galaxies and their Place in the Universe. SISSA, Trieste, PoS#34
Gallo L. C. et al., 2013, MNRAS, 428, 1191
Gallo L. C. et al., 2015, MNRAS, 446, 633
Gallo L. C., Blue D. M., Grupe D., Komossa S., Wilkins D. R., 2018, MNRAS, 478, 2557
Gallo L. C. et al., 2019, MNRAS, 484, 4287
Gierliński M., Done C., 2004, MNRAS, 349, L7
Gliozzi M., Williams J. K., 2020, MNRAS, 491, 532
Grier C. J. et al., 2012, ApJ, 755, 60
Grupe D., 2004, AJ, 127, 1799
Grupe D., Komossa S., Gallo L. C., 2007, ApJ, 668, L111
Grupe D., Komossa S., Gallo L. C., Fabian A. C., Larsson J., Pradhan A. K., Xu D., Miniutti G., 2008, ApJ, 681, 982
Grupe D., Komossa S., Leighly K. M., Page K. L., 2010, ApJS, 187, 64
Grupe D., Komossa S., Gallo L. C., Longinotti A. L., Fabian A. C., Pradhan A. K., Gruberbauer M., Xu D., 2012, ApJS, 199, 28
Grupe D., Gallo L., Komossa S., 2014, Astron. Telegram, 6468, 1
Grupe D., Longinotti A. L., Kriss G., Komossa S., Gallo L., Wilkins D., 2015, Astron. Telegram, 8477, 1
Grupe D., Komossa S., Gallo L., 2018a, Astron. Telegram, 11815, 1
Grupe D., Komossa S., Gallo L., Schartel N., 2018b, Astron. Telegram, 11835, 1
Grupe D., Komossa S., Gallo L., 2020, Astron. Telegram, 13757, 1
Hameury J. M., Viallet M., Lasota J. P., 2009, A&A, 496, 413
Hill J. E. et al., 2004, in Flanagan K. A., Oswald H. W., eds, Proc. SPIE Conf Ser. Vol. 5165, X-Ray and Gamma-Ray Instrumentation for Astronomy XIII. SPIE, Bellingham, p. 217
Jin C., Ward M., Done C., 2012, MNRAS, 425, 907
Kara E., Fabian A. C., Cackett E. M., Uttley P., Wilkins D. R., Zoghbi A., 2013, MNRAS, 434, 1129
Keek L., Ballantyne D. R., 2016, MNRAS, 456, 2722
Kelly B. C., Bechtold J., Siemiginowska A., 2009, ApJ, 698, 895
Kelly B. C., Bechtold J., Siemiginowska A., Aldcroft T., Sobolewska M., 2007, ApJ, 657, 116
King A. R., Pringle J. E., Livio M., 2007, MNRAS, 376, 1740
Komossa S., 2008, RMxAC, 32, 86
Komossa S., Grupe D., Saxton R., Gallo L., 2014, Styd. Conf, 143
Krawczyk C. M., Richards G. T., Mehta S. S., Vogeley M. S., Gallagher S. C., Leighly K. M., Ross N. P., Schneider D. P., 2013, ApJS, 206, 4
Longinotti A. L., Sim S. A., Nandra K., Cappi M., 2007, MNRAS, 374, 237
Longinotti A. L., Nucita A., Santos-Lleo M., Guainazzi M., 2008, A&A, 484, 311
Longinotti A. L. et al., 2013, ApJ, 766, 104
Longinotti A. L. et al., 2019, ApJ, 875, 150
Lusso E. et al., 2010, A&A, 512, A34
Lê S., Josse J., Husson F., 2008, J. Stat. Softw., 25, 1
Miniutti G., Fabian A. C., 2004, MNRAS, 349, 1435
Osterbrock D. E., Pogge R. W., 1985, ApJ, 297, 166
O'Neill P. M., Nandra K., Cappi M., Longinotti A. L., Sim S. A., 2007, MNRAS, 381, L94
Parker M. L. et al., 2014, MNRAS, 443, 1723
Parker M. L. et al., 2019, MNRAS, 490, 683
Park T., Kashyap V. L., Siemiginowska A., van Dyk D. A., Zezas A., Heinke C., Wargelin B. J., 2006, ApJ, 652, 610
Peterson B. M., Wanders I., Bertram R., Hunley J. F., Pogge R. W., Wagner R. M., 1998, ApJ, 501, 82
Poole T. S. et al., 2008, MNRAS, 383, 627
Porquet D., Reeves J. N., O'Brien P., Brinkmann W., 2004, A&A, 422, 85
R Core Team, 2013, R: A Language and Environment for Statistical Computing. R Foundation for Statistical Computing, Vienna, Austria, http://www.R-project.org/
Risaliti G., Young M., Elvis M., 2009, ApJ, 700, L6
Roming P. W. A. et al., 2005, Space Sci. Rev., 120, 95
Roming P. W. A. et al., 2009, ApJ, 690, 163
Ross N. P. et al., 2018, MNRAS, 480, 4468
Saez C., Chartas G., Brandt W. N., Lehmer B. D., Bauer F. E., Dai X., Garmire G. P., 2008, AJ, 135, 1505
Sarma R., Tripathi S., Misra R., Dewangan G., Pathak A., Sarma J. K., 2015, MNRAS, 448, 1541
Schlegel D. J., Finkbeiner D. P., Davis M., 1998, ApJ, 500, 525
Shemmer O., Brandt W. N., Netzer H., Maiolino R., Kaspi S., 2006, ApJ, 646, L29
Shemmer O., Brandt W. N., Netzer H., Maiolino R., Kaspi S., 2008, ApJ, 682, 81
Stern D. et al., 2018, ApJ, 864, 27

Strateva I. V., Brandt W. N., Schneider D. P., Vanden Berk D. G., Vignali C., 2005, AJ, 130, 387
Sun M. et al., 2020, ApJ, 891, 178
Tananbaum H. et al., 1979, ApJ, 234, L9
Tetarenko B. E., Lasota J. P., Heinke C. O., Dubus G., Sivakoff G. R., 2018, Nature, 554, 69
Vanden Berk D. E. et al., 2001, AJ, 122, 549
Vignali C., Brandt W. N., Schneider D. P., 2003, AJ, 125, 433
Wang J.-M., Watarai K.-Y., Mineshige S., 2004, ApJ, 607, L107
Wei T., Simko V., 2017, R package 'corrplot': Visualization of a Correlation Matrix. available at https://github.com/taiyun/corrplot
Wilkins D. R., Gallo L. C., 2015, MNRAS, 449, 129
Wilkins D. R., Gallo L. C., Grupe D., Bonson K., Komossa S., Fabian A. C., 2015, MNRAS, 454, 4440
Willingale R., Starling R. L. C., Beardmore A. P., Tanvir N. R., O'Brien P. T., 2013, MNRAS, 431, 394

SUPPORTING INFORMATION

Supplementary data are available at *MNRAS* online.

Table 2. *Swift* XRT and UVOT observations of Mrk 335 since 2018 February.
Table 3. *Swift* XRT and UVOT measurements of Mrk 335 since 2018 February.

Please note: Oxford University Press is not responsible for the content or functionality of any supporting materials supplied by the authors. Any queries (other than missing material) should be directed to the corresponding author for the article.

APPENDIX A: SPECTRAL ENERGY DISTRIBUTIONS OF INDIVIDUAL EPOCHS

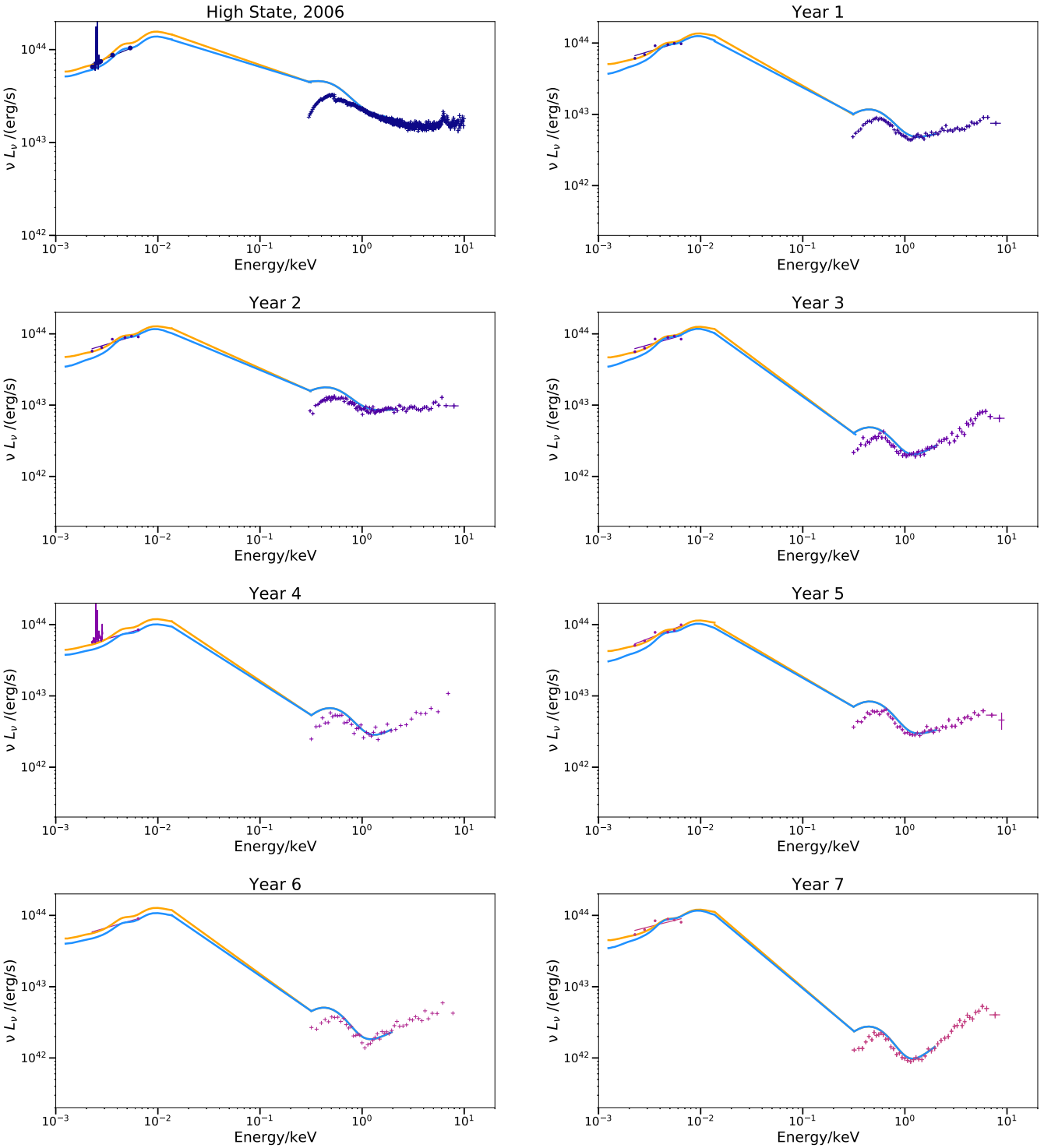

Figure A1. Spectral energy distribution measurements performed on individual epoch of 13-yr monitoring period of Mrk 335 are displayed. The modified Krawczyk SED, as described in Section 5, is applied to the data in each year of the 13-yr low state. The solid lines in yellow (with respect to 5100 Å normalization) and blue (with respect to 2500 Å normalization) show the integrated model used to evaluate bolometric luminosity for each epoch. Colours used for data in each SED diagram are consistent with Fig. 12.

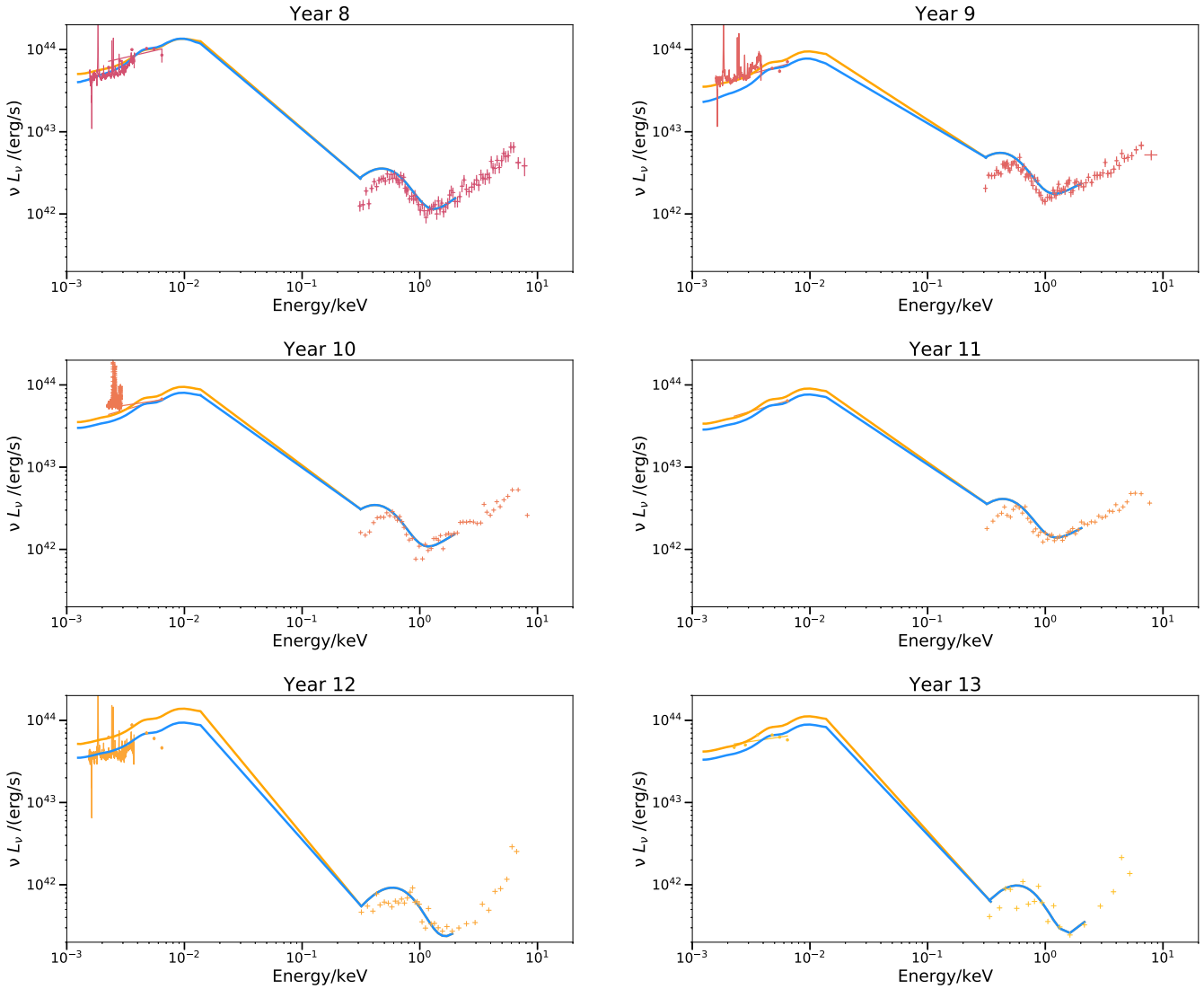

Figure A1 – *continued*.

This paper has been typeset from a TEX/LATEX file prepared by the author.